

## Whole Exome Sequencing Uncovers Key Genetic Variants in Congenital Tooth Agenesis: An Integrative Omics Approach

Prashant Ranjan<sup>a</sup>, Chandra Devi<sup>a</sup>, Neha Verma<sup>b,c</sup>, Rajesh Bansal<sup>b</sup>, Vinay Kumar Srivastava<sup>b</sup>, Parimal Das<sup>a,\*</sup>

<sup>a</sup>Centre for Genetic Disorders, Institute of Science, Banaras Hindu University, Varanasi, BHU-221005, UP, India

<sup>b</sup>Dentistry Oral Surgery and Medicine, Institute of Medical Sciences, Banaras Hindu University, Varanasi, BHU-221005, UP, India

<sup>c</sup>Dr Bhimrao Ramji Ambedkar Government Medical College, Kannauj, UP, India

\*Corresponding author

### Abstract

This study investigates the genetic underpinnings of congenital tooth agenesis (CTA) using a multi-omics approach, integrating whole exome sequencing (WES) and RNA expression analysis. WES was used to analyze the genetic basis of CTA in six affected individuals (one with syndromic and five with non-syndromic CTA) alongside three healthy and two internal controls. We identified both known and novel variants in candidate genes (*EDA*, *WNT10A*, *PAX9*, *TSPEAR*) and assessed the functional impacts of novel variants (*WNT10A* (A135S), and compound heterozygous *TSPEAR* (L219P, I419Lfs\*150)) using RT-PCR, while bioinformatics tools were applied to both known and novel variants. RT-PCR indicated disrupted *EDA* and *WNT10A* signaling in novel candidate genes *WNT10A* and *TSPEAR*. Computational analysis showed deleterious effects for six variants, with gene ontology, protein disorder, localization, and post-translational modifications suggesting significant functional changes. Molecular dynamics simulations predicted that these variants could impact protein stability and function. Additionally, WES analysis revealed 21 genes consistently present in all patients (MAF  $\leq$  20%), including novel variants in *OR4F21* (K310R, F44L) and *LCORL* (L1734P). Two variants, *OR4F21* (K310R) and *MRTFB* (A135A), appeared in all cases. Furthermore, 391 genes were shared among three patients, 204 among four, and 98 among five. Integrating multi-omic data from the GEO database identified 18 upregulated and 15 downregulated genes, with variants linked to systemic conditions such as autism, Alzheimer's, congenital heart disease (CHD), ALS (amyotrophic lateral sclerosis) and cancer. Our findings provide insights into CTA's molecular mechanisms, identifying potential biomarkers and therapeutic targets. Further validation could improve diagnosis and treatment strategies for CTA.

**Keywords:** Omics integration, Diseases association, Compound heterozygous, Bioinformatics, Molecular Dynamics.

## Abbreviations

**CTA** - Congenital Tooth Agenesis

**WES** - Whole Exome Sequencing

**GWAS** - Genome-Wide Association Studies

**OMIM** - Online Mendelian Inheritance in Man

**MAF** - Minor Allele Frequency

**qRT-PCR** - Quantitative Reverse Transcription Polymerase Chain Reaction

**CCDS** - Consensus Coding Sequence

**VUS** - Variants of Uncertain Significance

**AR**- Autosomal Recessive

**AD** - Autosomal Dominant

**XLR** - X-linked Recessive

**1CADD** - Combined Annotation Dependent Depletion

**OMIM** - Online Mendelian Inheritance in Man

**DEGs** - Differentially Expressed Genes

**SIFT** - Sorting Intolerant from Tolerant

**mCSM** - Mutation Cutoff Scanning Matrix

**DUET** - Dual Enrichment Testing

**PTMs**- Protein Translational Modification

**KEGG** - Kyoto Encyclopedia of Genes and Genomes

**RMSD** - Root Mean Square Deviation

**RMSF** - Root Mean Square Fluctuation

**Rg** - Radius of Gyration

**SAS** - Solvent-Accessible Surface Area

## 1. Introduction

Congenital tooth agenesis (CTA) is a developmental anomaly marked by the absence of one or more teeth, making it one of the most prevalent dental irregularities observed in humans. CTA is categorized based on the number of missing teeth: hypodontia involves the absence of one to five teeth (excluding third molars), oligodontia refers to the absence of six or more teeth, and anodontia denotes the complete absence of all teeth, which is extremely uncommon (Schonberger et al., 2023). CTA may present as a non-syndromic condition, occurring independently, or as a component of a syndromic disorder that also affects other ectodermal tissues, such as hair, nails, and sweat glands (Meade & Dreyer, 2023).

Non-syndromic congenital tooth agenesis (CTA) is estimated to affect around 8% of the global population, though prevalence rates vary widely by region. For example, some European studies have reported rates as low as 0.4%, reflecting the complex genetic factors influencing this condition (Galluccio et al., 2012). Inheritance patterns for non-syndromic CTA include autosomal dominant, autosomal recessive, and X-linked modes, highlighting its genetic heterogeneity (Yu et al., 2019).

Over the past few decades, various genes have been implicated in CTA. Early research identified mutations in genes such as *MSXI* and *PAX9*, both essential for tooth development, as key contributors to non-syndromic CTA. These genes are expressed in the dental mesenchyme and play a role in regulating other critical genes like *BMP4*, which is necessary for odontogenesis (Galluccio et al., 2012). Additionally, genes in the Wnt signaling pathway, including *WNT10A* and *AXIN2*, have been linked to CTA, with *AXIN2* mutations particularly associated with familial cases of oligodontia (Yu et al., 2019). The X-linked gene *EDA*, which is crucial for ectodermal development, has also been connected to both syndromic and non-syndromic tooth agenesis (Gao et al., 2023).

In our study, whole exome sequencing (WES) was employed to explore the genetic underpinnings of CTA. We analyzed exome data from six affected individuals (five with non-syndromic CTA and one with syndromic CTA), as well as three matched healthy controls and two internal family controls. This analysis revealed both previously reported and novel variants in candidate genes, including *EDA*, *WNT10A*, *PAX9*, and *TSPEAR*. Bioinformatics analysis were conducted to assess the potential functional impact of these variations. Our WES data identified 21 genes consistently present across all six patients, filtered based on a minor allele frequency

(MAF) of  $\leq 20\%$ . We also observed 391 genes shared among three patients, 204 among four patients, and 98 genes shared by five patients, which enabled us to refine a gene panel focused on genes identified in at least three CTA samples. To enhance our genetic findings, we integrated multi-omic data from the Gene Expression Omnibus (GEO) database, specifically examining syndromic CTA cases. This integrated approach revealed 18 upregulated and 15 downregulated genes from our WES panel. Our analysis identified three novel variants associated with tooth agenesis, along with several other gene variants previously unlinked to CTA but known to play roles in other conditions. These findings underscore the significant genetic contributions to congenital tooth agenesis, offering new insights that could improve diagnostic and therapeutic approaches. Enhanced genetic understanding may facilitate early diagnosis, enabling timely, targeted interventions that can improve outcomes for those affected by CTA.

## **2. Methodology**

### **2.1 Study Participants and Ethical Approval**

The Declaration of Helsinki's ethical standards were followed in this investigation. All participants or, in the case of minors, their parents or legal guardians, provided written informed consent. The Institute of Science's Ethics Committee of Banaras Hindu University in India examined and approved the research procedure. CTA patients were among the participants. Participation conditions were a verified diagnosis of CTA, being between the ages of 18 and 35, having complete dental records and radiographic images available, and having written consent from participants or their legal guardians. The exclusion criteria included a history of orthodontic treatment, inadequate dental records, or tooth loss due to non-congenital causes. The Institute of Medical Sciences, India's Department of Dentistry, Oral Surgery, and Medicine provided the five control samples and six patients for the study. The patients were booked for dental implant treatments after undergoing clinical evaluations. Five control subjects, who were all between the ages of 20 and 40, were chosen in order to closely resemble the patients' demographics. To maintain confidentiality and anonymity, each sample was assigned a unique study code.

### **2.2 Data Collection**

Dental records and radiographs of each participant were carefully examined to confirm the diagnosis and determine the extent of CTA. Clinical assessments were performed by qualified dental professionals to ensure the accuracy and consistency of data collection.

### **2.3 Blood Collection, Storage, and DNA/RNA Isolation**

Peripheral blood samples (1.5 mL) were collected using a 5 mL heparinized syringe and transported to the laboratory within 60 minutes, stored in a cooling box to preserve sample integrity. Genomic DNA was first extracted from these samples using the standardized salting-out method. The quality and quantity of the DNA were evaluated through spectrophotometric analysis (NanoDrop 2000, Thermo Scientific Inc.) or fluorometry-based methods, including the DNA Assay BR (Invitrogen, Cat# Q32853) and the Qubit High Sensitivity Assay (Invitrogen). For RNA isolation, 200  $\mu$ L of blood was processed using the Trizol reagent (Sigma-Aldrich, Catalog No. T9424). The concentration and purity of the extracted RNA were assessed using a NanoDrop spectrophotometer (Thermo Scientific, USA).

### **2.4 WES Analysis**

WES was conducted utilizing the Illumina Next-Generation Sequencing platform, focusing on approximately 30Mb of the human exome. This approach encompassed nearly 99% of the coding regions as defined by CCDS and RefSeq. Sequencing achieved a mean depth of 80-100X, with over 90% of the targeted regions covered at a minimum depth of 20X. To ensure data quality, duplicate reads were eliminated, and base quality recalibration was performed. The reads were mapped to the human reference genome GRCh38. Variant calling followed the GATK best practices, and subsequent variant annotation was carried out using databases such as OMIM, GWAS, gnomAD, and 1000 Genomes. Filtration of the annotated variants was based on several criteria, including a gnomAD allele frequency  $\leq 0.01$  or unavailable, a minimum read depth of 20, pathogenicity, and predicted functional consequences. Upon confirming the presence of the mutant variant in the candidate gene with a minor allele frequency (MAF) of  $\leq 0.01$ .

The WES analysis was conducted on a small Indian cohort consisting of 11 samples: 6 patient samples (DEN1, DEN10, DEN12, DEN20.1, DEN24.1, DEN23.1) and 5 controls, which included 3 healthy individuals and 2 internal controls. Notably, samples DEN1 and DEN12 were sourced from (Ranjan Jr et al., 2024; Sarkar et al., 2014). Initially, variants were filtered across

all samples using a Minor Allele Frequency (MAF) threshold of  $\leq 0.20$  to focus on rare variants that may be relevant to tooth agenesis. Following this, variants detected in control samples were subtracted from those found in the patient data, thus removing common variants likely unrelated to the condition.

Subsequent analysis involved identifying genes shared among different numbers of patients by examining the presence of variants across 3, 4, 5, or all 6 patient samples. This was accomplished using a combination of Excel and Python scripting to facilitate accurate comparison across datasets. Genes that appeared in at least 3 out of the 6 patient samples were selected to form the final WES gene panel, prioritizing those with a higher likelihood of being associated with tooth agenesis based on their recurrence across multiple patients.

## **2.5 Sanger Sequencing**

The salting-out technique was used to separate DNA from patient samples in order to verify new TSPEAR and WNT10A variations. Using certain primers, the TSPEAR and WNT10A sections were amplified by PCR and purified. Particular primers surrounding the target areas in TSPEAR and WNT10A were created and verified for the ideal melting temperature in order to perform Sanger sequencing. Initial denaturation at 95°C for 5 minutes, 30–35 cycles of 95°C for 30 seconds, primer-specific annealing at 55–60°C for 30 seconds, extension at 72°C for 45–60 seconds, and final extension at 72°C for 5 minutes were the processes used in PCR amplification. Following confirmation of the anticipated size on a 1.5% agarose gel, PCR products were purified to get rid of extra primers and nucleotides. The purified PCR products were subjected to Sanger sequencing using a sequencing dye terminator mix. Sequencing reactions included initial denaturation at 96°C for 1 minute, followed by 25–30 cycles of 96°C for 10 seconds, annealing at 50–55°C for 5 seconds, and extension at 60°C for 4 minutes. Sequencing reaction products were then purified and loaded onto a capillary electrophoresis instrument for analysis. Chromatograms were analyzed to confirm the presence of nucleotide changes, with mutant changes indicated by red arrows and unchanged nucleotides by green arrows Figure2.

## **2.6 RT PCR**

Blood samples from patients were used to extract total RNA, which was then measured using spectrophotometry to guarantee purity. Using oligo(dT) primers and the RevertAid First Strand

cDNA Synthesis Kit (Thermo Scientific, Catalog #K1622, USA), reverse transcription of mRNA was carried out in accordance with the manufacturer's instructions. The QuantStudio 6 Flex Real-Time PCR System from Applied Biosystems (Thermo Scientific, USA) was used to perform quantitative PCR (qRT-PCR). One microliter of cDNA (diluted 1:5), 6.25 microliters of Maxima SYBR Green/ROX qPCR Master Mix (2X, Thermo Scientific, Catalog #K0221, USA), one microliter of 10  $\mu$ M forward primer, one microliter of 10  $\mu$ M reverse primer specific for EDA or WNT10A, and nuclease-free water were all included in the 12.5 microliter reaction mixture. Following two minutes of initial denaturation at 95°C, 40 cycles of 95°C for 15 seconds and 60°C for 30 seconds comprised the qPCR cycling conditions. Primer blast utilized Primer designing. The  $\Delta$ CT technique was used to quantify relative expression levels after normalizing gene expression to an endogenous control (Beta-Actin).

## 2.7 Statistical Analysis

GraphPad Prism software (version 8; GraphPad Software, La Jolla, CA, USA) was used to conduct statistical analyses (Swift, 1997). To identify significant differences between groups, a one-way analysis of variance (ANOVA) was employed. To find particular group differences, post hoc comparisons were carried out using Tukey's multiple comparison test, with a significance threshold set at  $p < 0.05$ . The mean  $\pm$  standard deviation (SD) of the data was displayed.

## 2.8 Multiomics Integration:

**2.8.1 Data Sources and Gene Selection:** Differentially expressed genes (DEGs) were obtained from the study by (Ranjan Jr et al., 2024), using the GEO dataset ID **GSE56486**. This dataset was analyzed to identify genes that were significantly upregulated or downregulated. WES data was also utilized, comprising a gene panel with 709 genes relevant to congenital tooth agenesis.

**2.8.2 Identification of Common Genes:** To identify common genetic elements, the list of 709 WES genes was compared against the list of DEGs from the GSE56486 dataset. The comparison was performed using **Venny 2.0** (Oliveros, 2007), a widely-used tool for visualizing and identifying overlapping genes between datasets. Common genes between the WES panel and both upregulated and downregulated DEGs were identified, providing a focused set of targets for further analysis.

**2.8.3 Enrichment Analysis of WES Panel:** WES data was analyzed to identify genetic variants associated with congenital tooth agenesis. Variants from the WES panel were annotated and filtered based on established criteria, including allele frequency, functional impact predictions, and known associations with dental development. Following variant filtration, enrichment analysis was performed using Enrichr (E. Y. Chen et al., 2013), a comprehensive tool that allows for the functional characterization of gene lists. The analysis included pathways, biological processes, and disease ontology terms to determine if specific molecular pathways or biological functions were significantly overrepresented among the identified genes.

**2.8.4 Enrichment Analysis of Common Genes in DEGs:** Microarray-seq data analysis was used to identify differentially expressed genes (DEGs). To identify genes shared by the two datasets, genes exhibiting a significant differential expression ( $p$ -value  $< 0.05$ ) were compared to the WES panel. After that, Enrichr was used to do an enrichment analysis on the shared genes (E. Y. Chen et al., 2013). This method assisted in the identification of cellular components, molecular processes, and enriched biological pathways linked to the genes that exhibit both genetic variation and differential expression. The research offered a more thorough comprehension of the molecular pathways behind congenital tooth agenesis by combining the information from WES and DEGs.

### **2.8.5 PPI Network Construction and Analysis**

A list of 709 genes was examined using the STRING database (Szklarczyk et al., 2010) in order to look into the protein-protein interaction (PPI) network among the genes from the WES panel. The interaction score threshold was set to a high confidence level ( $\geq 0.4$ ) to ensure dependability when the genes were submitted to STRING in order to find known and anticipated interactions. Finding possible clusters and functional relationships within the network that could be connected to congenital tooth agenesis was the goal of this investigation. Then, using Cytoscape (Doncheva et al., 2018) a powerful tool for network visualization and analysis, the PPI network data from STRING was exported and loaded. After the network was further optimized within Cytoscape, interconnecting clusters and paths could be seen more clearly. The analysis included the calculation of topological parameters such as node degree, betweenness centrality, and clustering coefficients, which are essential for identifying key characteristics of the network structure.



**2.8.6 Hub Gene Identification:** To pinpoint central genes playing crucial roles within the PPI network, hub gene analysis was performed using **CytoHubba** (Chin et al., 2014), a plugin for Cytoscape. CytoHubba offers multiple algorithms to rank nodes based on their importance, using metrics such as **Degree, Betweenness, Closeness, and EPC (Edge Percolated Component)** scores. By applying these algorithms, the genes were ranked, and those with the highest centrality measures were identified as hub genes, indicating their potential key regulatory roles in the network.

The hub genes were visually highlighted within the PPI network, and sub-networks were extracted to focus on significant interactions involving these central nodes. This approach enabled the identification of core molecular interactions and pathways, providing deeper insights into the biological mechanisms that may contribute to congenital tooth agenesis.

## **2.9 Pathogenicity Prediction**

To predict the pathogenic potential of mutant proteins, we utilized a range of algorithm-based online tools, including SIFT (Vaser et al., 2016), PolyPhen-2 (Adzhubei & Jordan, n.d.), MutationTaster (Schwarz et al., 2010) and CADD (Rentzsch et al., 2019). Each tool required mutation-specific input, such as details of the amino acid substitution, and provided predictions based on distinct threshold and cutoff values.

## **2.10 Protein Stability Prediction**

We used a number of methods based on Gibbs free energy estimates to investigate how mutations affect protein stability. The stability changes linked to the mutant proteins were predicted using tools like mCSM (mutation cut off scanning matrix)(Pires et al., 2014b), DUET (Pires et al., 2014a), SDM (Worth et al., 2011) (Site Directed Mutator), SDM2 (Karnik et al., 2013), I-Mutant (Capriotti et al., 2005), MUpro (Parthiban et al., 2006), and the Cologne University Protein Stability Analysis Tool (CUPSAT)(Parthiban et al., 2006). These tools have different input requirements; mCSM, DUET, SDM, and CUPSAT require the protein's three-dimensional structure, whereas MUpro simply needs the amino acid sequence.

Additionally, I-Mutant was utilized to predict stability changes due to single-site mutations, with the tool capable of making predictions using either the protein sequence or structure based on SVM models.

## **2.11 Evolutionary Conservation Analysis**

Evolutionary conservation analysis was performed using the ConSurf web server (Glaser et al., 2003). The Position-Specific Iterative Basic Local Alignment Search Tool (PSI-BLAST) was used to identify homologous sequences for the EDA, WNT10A, PAX9, and TSPEAR protein sequences, selecting the top 150 sequences for further analysis. Conservation scores of amino acid residues were calculated by ConSurf, which applies Bayesian inference to evaluate evolutionary conservation. The scores range on a nine-point scale, where a score of 1 represents low conservation, indicating variable positions, and a score of 9 indicates high conservation, representing conserved regions.

### **2.12 Structural Analysis, Modeling, and Validation**

The 3D structures of PAX9, EDA, TSPEAR, and WNT10A proteins were obtained using AlphaFold(Jumper et al., 2021). Mutant models were generated through homology modeling based on AlphaFold templates (PAX9 AF-P55771-F1-v4, EDA AF-Q92838-F1-v4, TSPEAR AF-Q8WU66-F1-v4 and WNT10A AF-Q9GZT5-F1-v4) using the Swiss-Model webserver (Kiefer et al., 2009). To refine the models and minimize potential structural inconsistencies, energy minimization was performed using the "steepest descent" method with the GROMACS 2018 software suite (Berendsen et al., 1995). The quality and integrity of the modeled structures were further evaluated using the PDBsum tool (Laskowski et al., 2018).

### **2.13 RNA Sequence Retrieval**

The RNA sequences under analysis were sourced from the following transcript IDs: *WNT10A* NM\_025216, *EDA* NM\_001399, and *TSPEAR* NM\_144991. Short 41-nucleotide RNA segments were extracted with the mutation site precisely positioned at the 21st nucleotide having a sequence length of 20 bases on either side of the mutation site.

### **2.14 Prediction of RNA Secondary Structure**

For predicting the secondary structures (2D) of the RNA snippets, the RNAstructure Web Server (version 6.0.1) was employed(Devi, Ranjan, Raj, et al., 2024)(Bellaousov et al., 2013). This server utilizes algorithms grounded in thermodynamic principles to forecast RNA secondary structures. These predictions elucidate folding patterns and potential base pairing interactions within the RNA molecules.

### **2.15 Assessment of Mutation Effects on RNA Structure**

To explore the structural alterations induced by each missense mutation, the MutaRNA tool facilitated the mutational analysis of RNA sequence (Miladi et al., 2020). This analysis encompassed evaluating the intra-molecular base pairing potential, determining base pairing probabilities of the mutant RNA, and assessing accessibility (single-strandedness) in comparison to the wild-type counterparts (Miladi et al., 2020)(Bernhart et al., 2011). By incorporating remuRNA (Salari et al., 2013) and RNAsnp, this tool provides insights into the mutation-induced changes in RNA structures.

## **2.16 Prediction of Post-Translational Modifications (PTMs)**

To identify potential PTMs in proteins, various computational tools were used. NetPhos 3.1(Blom et al., 1999) predicted phosphorylation sites (serine, threonine, tyrosine), while NetNGlyc (Pugalenthi et al., 2020) and NetOGlyc(Hansen et al., 1998) identified N- and O-glycosylation sites, respectively. GPSSNO(Xue et al., 2010) was employed for S-nitrosylation prediction, and GPSSUMO (Zhao et al., 2014) identified sumoylation sites and motifs. PrePS analyzed prenylation types, including farnesylation and geranylgeranylation (Maurer-Stroh & Eisenhaber, 2005). UbPred(Radivojac et al., 2010) predicted ubiquitination sites, Myristoylator identified N-terminal myristoylation, and CKSAAPPalm (Ranjan & Das, 2023) along with eqPalm were used for palmitoylation. Finally, GPS PAIL (Deng et al., 2016) predicted lysine acetylation sites. Each tool relied on protein sequence inputs to detect possible modifications, providing insights into how these PTMs might regulate protein function and stability, with implications for congenital tooth agenesis.

## **2.17 Molecular Simulations**

GROMACS was used to perform molecular dynamics (MD) simulations in order to examine the structural behavior of the wild-type and mutant forms of the proteins PAX9, EDA, TSPEAR, and WNT10A. For these simulations, the GROMOS96 54a7 force field (Schmid et al., 2011)(Devi, Ranjan, & Das, 2024) was used. SPC216 water molecules were used to encircle the proteins in a dodecahedron box arrangement, with the proteins and box edges spaced at least 1.0 nm apart. In order to simulate physiological circumstances, 0.15 M NaCl and Na ions were added to electrically neutralize the system.

The steepest descent approach was used to minimize energy and resolve any steric conflicts. Subsequently, the system underwent two stages of equilibration: first, at 300 K, under the NVT ensemble (constant number of particles, volume, and temperature); and secondly, at 1 atm for 100 ps, under the NPT ensemble (constant number of particles, pressure to temperature). MD simulations were prolonged to a period of 50 ns following the equilibration phases. All mutant and wild-type structures achieved a stable equilibrium state within 10 ns. GROMACS tools (e.g., gmx rms, rmsf, gyrate, hbond, and sas) were used to analyze key parameters, such as solvent-accessible surface area (SAS), hydrogen bonds (intra-protein and protein-water interactions), radius of gyration (Rg), root mean square deviation (RMSD), and root mean square fluctuation (RMSF). The results were visualized using XMGRACE (Cowan & Grosdidier, 2000) and MS excel (Berk & Carey, 1998).

### **2.18 Principal Component Analysis (PCA) of Biophysical Metrics and Matplot analysis**

To assess and visualize variability among different protein variants, we conducted Principal Component Analysis (PCA) based on key biophysical metrics: root mean square deviation (RMSD), root mean square fluctuation (RMSF), solvent-accessible surface area (SAS), hydrogen bond count (H-bonds), radius of gyration (Rg), and subcellular localization properties. These metrics were measured for a variety of wild-type and mutant proteins, including EDA (EDA\_WT, EDA\_R156H), PAX9 (PAX9\_WT, PAX9\_Q145\*), TSPEAR (TSPEAR\_WT, TSPEAR\_419fs150, TSPEAR+Compound\_Hetero), and WNT10A (WNT10A\_WT, WNT10A\_V145M, WNT10A\_A135S).

To ensure fair comparison, the data were standardized, allowing each feature to contribute equally to the analysis and preventing any single metric from dominating the results. PCA was performed using the scikit-learn library (Kramer, 2016), reducing the dataset to two principal components (PC1 and PC2) that captured most of the variance.

The PCA results were visualized as a scatter plot, where each point represented a protein variant. Different colors and annotations were used to distinguish between the variants, facilitating easy identification of patterns and clusters. The protein variant analysis was conducted using Python (v3.12) (Python, 2021) with pandas for data management and matplotlib (Hunter & Dale, 2007) for visualization. The biophysical metrics (RMSD, RMSF, SAS, H-Bonds, Rg) were plotted across the different protein variants using subplots. Distinct colors and triangular markers were employed for each metric, enhancing clarity and comparison.

### **2.19 Others relevant miscellaneous analysis**

For the analysis of protein variants, several computational tools were employed. Secondary structure prediction and Gene Ontology (GO) annotations for wild-type and variant forms of PAX9, EDA, WNT10A, and TSPEAR were performed using the Psipred Workbench (Buchan & Jones, 2019). The protein sequences served as input for these predictions, providing insights into structural changes and functional implications associated with each variant. The difference distance matrix and Root Mean Square Deviation (RMSD) calculations were conducted using Superpose Version 1.0 (Bauer et al., 2008), enabling a detailed comparison of structural variations between the wild-type and mutant proteins. Additionally, TBtools (C. Chen et al., 2020), a versatile toolkit for biological data analysis, was utilized to generate heat maps, offering a clear visualization of the data across multiple metrics. Subcellular localization of the wild-type and variant proteins (PAX9, EDA, WNT10A, TSPEAR) was predicted using DeepLoc 2.0 (Thumuluri et al., 2022). Protein sequences were submitted to the DeepLoc 2.0 web server, which employs a convolutional neural network to predict localization probabilities for various cellular compartments (e.g., nucleus, cytoplasm, mitochondria). The predictions were analyzed to identify the most likely localizations for each variant, and results were visualized for comparative analysis.

Discover Studio (Systèmes, 2016) was used for detailed structural analysis, providing insights into the biophysical properties of each protein variant.

### 3 Result

#### 3.1 WES Analysis

The WES analysis of CTA patients identified several variations in candidate genes linked to tooth agenesis. In *WNT10A*, a homozygous variation V145M (c.433G>A) was found, classified as likely pathogenic with autosomal recessive (AR) inheritance, and is a known variant. Additionally, a heterozygous novel variant A135S (c.403G>T) was identified as a variant of uncertain significance (VUS) associated with autosomal dominant (AD) inheritance. For *EDA*, a known homozygous variant R156H (c.467G>A), classified as likely pathogenic, was observed, linked to ectodermal dysplasia and X-linked recessive (XLR) inheritance. In *PAX9* a stop-gained mutation (c.433C>T; p.Gln145\*), classified as pathogenic, known, and related to AR inheritance. In *TSPEAR*, two compound heterozygous variations were identified: L219P (c.656T>C), a novel VUS with autosomal recessive (AR) inheritance, and a frameshift variant I419Lfs\*150 (c.1255delA), classified as a known VUS. These findings provide insights into the

genetic basis of tooth agenesis, highlighting both known pathogenic variants and novel uncertain variants for further investigation (**Table 1, Figure1**). Further Novel variants cross validated by sanger sequencing showed in Figure2.

The variant analysis summarized here corresponds to the findings presented in **Table 2**. Each variant, including *TSPEAR* (L219P and I419fs150), *PAX9* (Q145\*), *WNT10A* (A135S and V145M), and *EDA* (R156H), has been assessed across multiple databases and predictive tools. The results indicate their potential pathogenicity, with entries in databases like OMIM, EXAC, and gnomAD, along with consistent damaging predictions from tools such as SIFT, Polyphen-2, MutationTaster2, and CADD3 Phred scores.

### 3.2 RT-PCR Assessment of Novel Variants Affecting Wnt and EDA Signaling

RT-PCR analysis revealed significant reductions in the expression levels of *EDA* and *WNT10A* in samples carrying the identified variants. Specifically, *EDA* expression was notably decreased compared to the internal control (Figure 2. G), with  $\Delta$ CT values indicating substantial downregulation. Similarly, *WNT10A* expression was significantly lower in variant samples (Figure 2. H), further supported by the  $\Delta$ CT values. Statistical analysis confirmed these findings, with \*\*\*\*p < 0.0001 for *EDA* and \*\*\*p < 0.001 for *WNT10A*, indicating that the identified variants adversely affect EDA and WNT signaling pathways, potentially contributing to the observed phenotypes.

### 3.3 WES Gene Panel

Data from five control samples and six CTA patients were filtered using a minor allele frequency (MAF) criterion of  $\leq 20\%$  as part of the full WES analysis. The emphasis was on possible related genes unique to the CTA patients by excluding common variations using those found in the control samples. 709 genes made up the final curated gene panel that was discovered using this method. Of the genes in the panel, 21 are consistently seen in all six patients, 391 are shared by three patients, 204 are found in four patients, and 98 are seen in five patients. By giving priority to genes found in more than three CTA samples, the gene panel was improved in terms of specificity and CTA relevance.

Gene panel showed in Supplementary File Information S2. Ten genes (*TM4SF20*, *LCORL*, *OR4F21*, *TNS2*, *VWA8*, *MYH6*, *KNL1*, *LOC400499*, *MRTFB*, and *PRR32*) contained mutations categorized as synonymous, non-synonymous, or found in UTR sections, according to a

thorough study of variants present in 21 genes shared by all six patient samples. This analysis did not include variants that fell outside of these categories (Table 3). Diverse conclusions were drawn from the examination of variations in ten genes that were present in six patient samples. Variants in *MYH6* (G56R) and *TM4SF20* (A27V) were found to be benign, had moderate minor allele frequencies (MAF), and were present in several samples, indicating that they were common.

*LCORL* revealed three variations, including a benign synonymous variant (T1042) that was found in several samples and two variants of unclear significance (VUS) L1734P (new) and P1709R (rare), suggesting possible variation in regulatory functions. Two novel VUS (K310R, F44L) were found in *OR4F21* across samples, suggesting unique variants of unknown importance. There were two non-synonymous variations found in *TNS2* (I858M and G774E), the former of which was categorized as VUS and the latter as benign. With modest MAFs, the *VWA8* (R552H, I1439L) and *PRR32* (M193T) variants were likewise innocuous.

Although there was no clinical categorization information available, *LOC400499* had two non-synonymous variations (G2806R, I176V), and *KNLI* displayed a rare VUS (A1270V). A harmless synonymous variation (A135) of *MRTFB* was found in several samples, indicating a shared polymorphism. All things considered, the study found both new and benign VUS variations, offering information on the genetic causes of a number of illnesses. *TM4SF20* (autism, Alzheimer's), *LCORL* (growth disorders, Alzheimer's), *OR4F21* (no known diseases), *TNS2* (kidney diseases), *VWA8* (COVID-19, cleft lip palate, autism), *MYH6* (congenital heart disease (CHD)), *KNLI* (microcephaly), *LOC400499* (unknown), *MRTFB* (autism, CHD), and *PRR32* (intellectual development disorders) were among the gene-disease associations found by the analysis.

These correlations point to possible genetic causes of the disorders seen in the patient samples. In all six samples, two variations were consistently found: *MRTFB* (A135, c.405T>C) and *OR4F21* (K310R, c.929A>G). Whereas the *MRTFB* variation is a known synonymous alteration, the *OR4F21* variant is a new, non-synonymous modification.

Key pathways and functions were discovered by the WES panel's enrichment analysis (Figure 3). Pathway study revealed important roles in apoptotic signaling, cell cycle control, and DNA damage response. Protein localization to membranes and DNA replication and repair were examples of biological activities that suggested roles in cellular growth and stability. Mitochondrial complexes, CMG complexes, and cell junctions were found to be abundant in

cellular components, indicating their significance in energy metabolism, DNA synthesis, and cell communication. DNA binding, helicase activity, and oxidoreductase activity were the main molecular activities that were linked to enzymatic processes and genomic stability. Human phenotypic ontology revealed links to diseases such as myelodysplasia and bone marrow hypoplasia, suggesting genetic susceptibilities to hematological and developmental disorders.

The PPI network analysis of the WES gene panel identified 470 nodes and 1211 interactions, showing a well-connected network structure (**Figure 4 Panel A**). The analysis revealed 11 network modules with key hub genes, including *TNF*, *TP53*, *STAT3*, and *CXCL12* (**Figure 4 Panel C**), indicating their central role. Yellow-highlighted genes within the network represent those associated with developmental processes, suggesting their relevance in tooth development. Summary metrics (**Figure 4 Panel B**) showed an average of 5.153 neighbors per node, a clustering coefficient of 0.126, and a network density of 0.005.

### 3.4 Multiomics Integration

The multi-omics integration analysis revealed shared gene elements across the WES Panel, GSE56486\_UP, and GSE56486\_Down datasets. The Venn diagram showed 676 unique genes in the WES Panel, 726 in GSE56486\_UP, and 60 in GSE56486\_Down, with 18 genes common between the WES Panel and GSE56486\_UP, and 15 shared between the WES Panel and GSE56486\_Down. The heatmap of the 18 common genes suggests possible functional or regulatory relationships. KEGG pathway analysis indicated that upregulated genes were enriched in pathways like NOD-like receptor signaling, steroid biosynthesis, and cytoskeletal metabolism, while downregulated genes were linked to pathways involving endocytosis, bacterial invasion of epithelial cells, and fatty acid degradation, hinting at disruptions in cellular metabolic activities (**Figure5**).

The functional analysis integrating WES panel data with differentially expressed genes (DEGs) shows that upregulated genes are primarily associated with binding activities and enzymatic functions, while downregulated genes are linked to oxidoreductase activities, cytoskeletal binding, and ion transport. On the cellular level, upregulated genes contribute to extracellular matrix components, ion transport, and adhesion, whereas downregulated genes are connected to cell junctions, protein complexes, and cytoskeleton components. In terms of biological function, upregulated genes are enriched in processes like cell adhesion, signal transduction, and vascular development, while downregulated genes are focused on cell proliferation, immune response, and metabolism (**Figure5**). A comprehensive analysis of 33 differentially expressed genes



(DEGs) revealed several notable variants. Among these, *ENAH* exhibited a benign deletion variant (ERQERLD217D) in samples DEN1 and DEN20.1. *LOX* showed a benign non-synonymous variant (R158Q) with a minor allele frequency (MAF) of 17.02%. *NR3C1* and *TIMP2* presented synonymous changes, while *IRF5*, *CEL* (novel), and *ABTB2* had variants classified as variants of uncertain significance (VUS). Additionally, *RNF175*, *TGFB1*, and *PRKCB* presented benign and VUS variants across multiple samples, contributing to the understanding of genetic factors associated with various diseases. Further insights can be gleaned from the detailed **Table4**.

### 3.5 Diseases Association

The genetic variants identified in patients with tooth agenesis show associations with several systemic diseases. *TM4SF20*, involved in cell adhesion, has been linked to autism and AZ. *LCORL*, a transcriptional regulator, is associated with growth development disorders, AZ, and autism. *OR4F21*, an olfactory receptor gene, presents novel variants but has no reported disease associations. *TNS2*, associated with kidney diseases, harbors mutations that could impact cell migration, possibly contributing to nephropathy and other organ-related conditions. *VWA8*, involved in extracellular matrix stability, is associated with COVID-19, cleft lip palate, and autism. *MYH6*, related to cardiac muscle function, is linked to CHD. The role of cellular division and mitosis in tooth and brain development is supported by *KNLI*, which is linked to microcephaly and cancer. A putative protein called LOC400499 may have important but unidentified roles in systemic illnesses. Autism and congenital heart disease are linked to *MRTFB*, which is involved in transcription and cell signaling. Lastly, there is more evidence linking neurological issues to tooth growth through *PRR32*, which is linked to intellectual development difficulties.

The integrity of the extracellular matrix depends on the cross-linking of collagen and elastin, which is catalyzed by the *LOX* gene (lysyl oxidase). It has a connection to ALS. The *LOX* R158Q variation, which occurs 17.02% of the time, is categorized as benign. This variation, which was shown to be among the top 10 hub genes, results in a non-synonymous coding mutation due to a nucleotide change at c.473G>A. Three patient samples include *LOX*.

### 3.6 Relative Entropy

The relative entropy scores ( $H(\text{wt}:\mu)$ ) computed by remuRNA in mutaRNA analysis for each coding sequence change in the investigated genes provides the information of structural impact of single nucleotide change within RNA sequences. These are summarized in Supplementary Information S1. The higher the relative entropy value, the stronger the structural impact of the nucleotide-change on the RNA structure. The variant *WNT10A* c.403G>T stands out with a higher relative entropy score of 3.409, suggesting a substantial alteration in RNA structure compared to other variants examined followed by *EDA* c.467G>A variant and *TSPEAR* c.656T>C exhibiting relatively high entropy scores of 2.248 and 1.392, respectively, indicating notable structural impacts. In contrast, the *WNT10A* c.433G>A variant reports a lower relative entropy score of 0.355, suggesting a comparatively lesser impact on RNA structure.

### 3.7 Analysis of RNA structural features

Further analysis of the variants' impact on RNA structural features revealed distinct impacts of single nucleotide polymorphisms (SNPs) on the wild type (WT) and mutant (MT) RNA sequences. The results indicate that the variant *WNT10A* c.403G>T has the most pronounced effect on RNA structure, followed by *TSPEAR* c.656T>C, whereas minor alterations are observed in *WNT10A* c.433G>A and *EDA* c.467G>A (Figure 6, 7). Similarly, these alterations in the base pairing probabilities and change in structure can be observed in 2D structures of WT and MT depicted in Supplementary Information S1. In Figure 6, heat map dot plots illustrate the base pairing potential of both WT and MT RNAs, with darker color dots indicating higher probabilities of base pairing. Circular plots depict the same base pair probabilities, with darker hues of grey indicating higher probabilities. Analysis of changes in base pair probabilities, as shown in Figure 6 ( $\text{Pr}(\text{bp in WT}) - \text{Pr}(\text{bp in mut})$ ), highlights difference in base pairing patterns between WT and MT RNAs at specific locations. The weakened base pairing potential and increased probabilities of base pairing within each MT RNA are depicted in Figure 7.

The accessibility profiles, as depicted in Figure 6, reveal varying effects of the examined variants on RNA. The accessibility profiles are assessed based on RNA single-strandedness (unpaired probabilities), representing the likelihood of each nucleotide position being unpaired within the RNA sequences. It is a crucial factor influencing RNA-protein or RNA-RNA interactions. Notably, the variant *WNT10A* c.403G>T exhibits the most pronounced alteration in accessibility, following closely, the variant *TSPEAR* c.656T>C also shows notable changes in accessibility profiles, indicating an impact on RNA single-strandedness. In contrast, minor alterations in accessibility profiles are observed for the variants *WNT10A* c.433G>A and *EDA*

*c.467G>A*, reflecting relatively lesser effects on RNA structure compared to the former variants as depicted in Figure 6.

### **3.8 Evolutionary Conservation of Candidate gene variations.**

The conservation analysis (**Figure 8**) revealed that several variants, including TSPEAR L219P, WNT10A A135S, WNT10A V145M, and EDA R156H, are located in highly conserved regions with a conservation score of 9 out of 9, indicating strong evolutionary stability. TSPEAR L219P showed a slightly lower conservation score of 8. Variants such as PAX9 Q145\* and TSPEAR I419fs\*150 lead to truncations or frameshifts, resulting in the absence of significant portions of the protein. Notably, these disrupted regions consist of amino acids that are highly conserved, suggesting their critical functional importance.

### **3.9 Protein Structure Stability Analysis**

The stability analysis of gene variants (**Table 5**) revealed that TSPEAR L219P, WNT10A A135S, WNT10A V145M, and EDA R156H predominantly show destabilizing effects across multiple prediction tools, indicating a decrease in protein stability. For TSPEAR L219P, all tools consistently predicted a destabilizing impact, with  $\Delta\Delta G$  values ranging from -1.284 to -5.93 kcal/mol. WNT10A A135S showed significant destabilization across all models, particularly in DUET (-2.606 kcal/mol). WNT10A V145M had mixed predictions, with most tools indicating destabilization except CUPSAT, which predicted stabilization (0.98 kcal/mol). EDA R156H presented a slight destabilizing trend, with I-Mutant showing the most substantial decrease (-1.20 kcal/mol). Variants TSPEAR I419fs\*150 and PAX9 Q145\* could not be assessed for stability due to their truncating nature.

### **3.10 Structural and Functional Analysis of Variants**

The tertiary structure analysis showed stability in the case of non-synonymous variants. However, for TSPEAR, the structural comparison of compound heterozygous variants with distance matrix plot, as shown in Figure 9, revealed notable alterations. The secondary structure analysis (Figure 10) revealed structural alterations across the WNT10A, TSPEAR, and EDA genes due to specific mutations. In WNT10A, the novel variant p.A135S and the known variant p.V145M both showed changes in helices and strands compared to the wild-type, suggesting potential impacts on the protein's stability and function. For TSPEAR, the variant p.L219P and the frameshift mutation p.Ile419Lfs\*150 indicated disruptions in transmembrane helices and signal peptides, which may affect protein localization and signaling. In EDA, the p.R156H

variant showed alterations in metal-binding and extracellular domains, pointing to possible functional changes. These structural differences highlight how mutations can affect protein conformation and biological activity.

The protein disorder prediction (Figure 11) analysis showed differences between wild-type and mutant forms across the WNT10A, TSPEAR, and EDA genes. For WNT10A, both the known variant (p.V145M) and the novel variant (p.A135S) exhibited alterations in disordered regions. TSPEAR variants, including p.L219P and the frameshift mutation (p.Ile419Lfs\*150), showed shifts in disorder profiles. In EDA, the p.R156H mutant displayed changes in disordered segments.

The GO enrichment analysis of the variants (Figure 12-15), compared to the wild type, revealed changes in the functional roles of the affected proteins. Variants showed alterations in biological processes, molecular functions, and cellular components, indicating shifts in protein behavior and potential impacts on associated pathways. PTM analysis (Figure 16) revealed functional alterations in TSPEAR (p.I419F), compound heterozygous TSPEAR, WNT10A (p.A135S), PAX9 (p.Q145\*), and EDA (p.R156H) variants. Subcellular localisation analysis (Figure 17) indicated that most variants exhibit similar localization patterns to the wild-type. However, TSPEAR variants displayed distinct shifts, suggesting potential impacts on functionality.

Hydrophobicity changes (Supplementary Information1) among protein variants. WNT10A variants (p.A135S, p.V145M) have slight decreases compared to wild type. PAX9 p.Q145\* displays increased hydrophobicity. TSPEAR variants (p.L219P, compound heterozygous) show variable changes. EDA p.R156H has a marked increase, suggesting altered structural properties.

### 3.11 Molecular Simulation Dynamics Analysis

The molecular dynamics simulations (**Figure 18-22**) conducted over a period of 10 ns revealed that the protein variants reached equilibrium, providing valuable insights into their structural stability and flexibility. RMSD showed the highest deviation in EDA\_R156H (3.073 Å), while WNT10A\_WT had the lowest (0.128 Å), indicating structural stability. RMSF was highest in EDA\_R156H (1.106 Å) and TSPEAR\_Compound\_Hetero (0.675 Å), suggesting increased flexibility. SAS showed a significant increase in EDA\_R156H (124.049 Å<sup>2</sup>), while WNT10A variants remained stable. H-bond counts were lower in EDA and TSPEAR variants, with TSPEAR\_Compound\_Hetero at 250.722 compared to TSPEAR\_WT (421.84). Rg was highest for TSPEAR\_Compound\_Hetero (2.349 Å), indicating an expanded structure. The comparative

analysis of protein dynamics revealed distinct clustering of variants. Variants plotted close to each other on the PCA plot (**Figure 22**) indicated similar biophysical characteristics, while those positioned further apart suggested significant differences due to mutations. Notable insights from the PCA plot included the clustering of *WNT10A* wild-type and its variants (V145M, A135S), which indicated minimal changes in their biophysical properties. In contrast, *TSPEAR* variants, including *TSPEAR\_419fs150* and *TSPEAR+ Compound Hetero*, were distinctly separated from *TSPEAR\_WT*, suggesting significant alterations in their profiles due to mutations. Additionally, the *EDA\_R156H* and *PAX9\_WT* variants displayed greater dispersion compared to their wild-type counterparts, indicating potential structural or functional changes resulting from the mutations. The overall wider spread of points across the plot highlighted the diversity of the variants, with isolated points, such as *EDA\_R156H*, likely indicating substantial changes in structure or dynamics. Matplotlib, providing a clear representation of the dynamic properties of the simulated variants (**Figure 22**).

#### 4 Discussion

This study provides an in-depth genetic analysis of congenital tooth agenesis (CTA) by using whole-exome sequencing (WES) and integrating omics data to reveal key genetic variants and their functional impacts. The results identify both known pathogenic variants and novel variants of uncertain significance (VUS), contributing valuable insights into the molecular mechanisms underlying CTA. Significant genetic diversity was observed, with variants identified in key CTA candidate genes, including *WNT10A*, *EDA*, *PAX9*, and *TSPEAR*, among others. This diversity highlights the heterogeneity and complex inheritance patterns characteristic of this condition. Our approach emphasizes the value of WES as a diagnostic and research tool for rare congenital disorders and highlights the functional consequences of specific gene alterations on signaling pathways critical for tooth development.

The WES analysis identified key genetic variants linked to CTA, especially in *WNT10A*, *EDA*, *PAX9*, and *TSPEAR*. This study highlights both known pathogenic and novel variants of uncertain significance (VUS), reflecting the genetic diversity and complex inheritance patterns involved in CTA. Using variant analysis tools and databases like OMIM, EXAC, and gnomAD, the pathogenicity of these variants was consistently supported, providing valuable insights into CTA's genetic basis.

In *WNT10A*, a homozygous V145M (c.433G>A) variant, classified as likely pathogenic, underscores the critical role of WNT signaling in tooth development. *WNT10A* has previously been associated with several ectodermal dysplasia syndromes that manifest with tooth agenesis, highlighting its influence on ectodermal organogenesis (Bohring et al., 2009). This autosomal recessive (AR) variant aligns with previous studies indicating that *WNT10A* homozygous mutations often lead to more severe phenotypes, such as oligodontia and hypodontia (van den Boogaard et al., 2012). Additionally, the heterozygous novel variant A135S (c.403G>T), classified as a VUS with autosomal dominant (AD) inheritance, introduces a potential new dimension to the inheritance pattern of *WNT10A*-related agenesis. The presence of this variant as a VUS suggests possible gene-environment interactions or oligogenic contributions that may modify its penetrance and expressivity in CTA phenotypes.

The *EDA* gene variant R156H (c.467G>A), found in a homozygous form and linked to X-linked recessive (XLR) inheritance, is classified as likely pathogenic and highlights the role of ectodysplasin A signaling in ectodermal tissue development. Mutations in *EDA* are well-documented in ectodermal dysplasias, often affecting multiple ectodermal structures, including teeth (Cardoso et al., 2021). This variant's association with tooth agenesis further validates the role of *EDA* in CTA, with consistent damaging predictions across SIFT, Polyphen-2, and MutationTaster2 indicating a probable disruptive effect on *EDA* signaling. Since *EDA* mutations typically follow XLR inheritance, this variant could contribute to CTA, particularly in male patients who are hemizygous for the mutation.

The *PAX9* gene, which encodes a transcription factor crucial for tooth development, also exhibited two variants. A stop-gain mutation, Q145\* (c.433C>T), classified as pathogenic with AR inheritance, is consistent with prior findings that pathogenic *PAX9* mutations contribute to non-syndromic oligodontia (Bonczek et al., 2017). Additionally, a novel VUS (c.-31C>A), associated with AD inheritance, further complicates the genetic picture in CTA. The AD VUS may suggest a less severe or subclinical phenotype, indicating that not all *PAX9* mutations manifest with complete penetrance in CTA. Such variants emphasize the importance of considering diverse inheritance models when evaluating CTA's genetic etiology, as heterozygous variants in *PAX9* may also impact dental development in a dose-sensitive manner.

The *TSPEAR* gene cause both Syndromic and non-Syndromic CTA(Du et al., 2018)(Peled et al., 2016). The identification of heterozygous variants in the *TSPEAR* gene in both affected siblings, with one variant inherited from an unaffected mother, raises critical questions about the gene's

role in disease pathology. TSPEAR is associated with developmental processes, and haploinsufficiency has been linked to phenotypic manifestations in affected individuals. The presence of two variants—L219P (c.656T>C) and a frameshift mutation I419Lfs150 (c.1255delA)—suggests that compound heterozygosity may contribute to the clinical phenotype.

The second variant may be a de novo mutation or be inherited from the father, whereas the first variant is transmitted from the mother. Because the I419Lfs150 frameshift mutation results in a shortened protein, it may alter its function and impact ectodermal structures, which is important for diseases like tooth agenesis. The relevance of assessing both hereditary and de novo mutations in genetic evaluations is highlighted by the possibility that both variations, although being categorized as variants of unknown significance (VUS), may jointly contribute to the phenotype.

In order to clarify these variations' contributions to CTA and improve our knowledge of the genetic foundation of this disorder, more functional research is required to determine how these variants affect TSPEAR activity and their function in dental epithelial signaling. Further functional validation is necessary to ascertain if the defective TSPEAR protein affects tooth epithelial signaling, since the compound heterozygous presentation implies that both alleles contribute to the phenotype.

All identified variants were assessed across predictive tools, including SIFT, Polyphen-2, MutationTaster2, and CADD3 Phred scores, all of which indicated damaging effects for pathogenic variants in *WNT10A*, *EDA*, *PAX9*, and *TSPEAR*. This consistent pathogenicity prediction across tools and databases strengthens the evidence that these variants likely contribute to CTA. The use of multiple databases, such as OMIM, EXAC, and gnomAD, allowed us to cross-reference allele frequencies and variant classifications, enhancing the robustness of our analysis. Specifically, the presence of these variants in disease-associated databases and their classification as likely damaging through computational models underscores the relevance of these candidate genes in CTA pathogenesis.

The RT-PCR analysis reveals that variants in *EDA* and *WNT10A* significantly reduce the expression levels of these genes in CTA samples. Specifically, *EDA* expression showed marked downregulation, with  $\Delta$ CT values reflecting substantial decreases relative to the internal control ( $p < 0.0001$ ). Similarly, *WNT10A* expression was also notably diminished in samples carrying the variants ( $p < 0.001$ ), suggesting a direct impact of these mutations on WNT and EDA signaling pathways. This downregulation supports the hypothesis that impaired WNT and EDA

signaling contributes to tooth agenesis by disrupting essential pathways in ectodermal tissue development. Prior studies emphasize the roles of *EDA* and *WNT10A* in regulating ectodermal differentiation, further validating their association with phenotypes seen in CTA (Bohring et al., 2009)(Cardoso et al., 2021).

This WES gene panel analysis has identified a curated set of 709 genes with potential relevance to congenital CTA, providing critical insights into the genetic underpinnings of this condition. By filtering variants with a minor allele frequency (MAF) threshold of  $\leq 20\%$  and comparing patient-specific variants against controls, the study narrowed down candidate genes that may influence CTA. The final gene panel includes both rare variants of uncertain significance (VUS) and benign variants, offering a comprehensive view of both potential pathogenic contributors and common polymorphisms in CTA.

Among the 21 genes commonly present in all patient samples, variants in *TM4SF20*, *LCORL*, *OR4F21*, *TNS2*, *VWA8*, and *MYH6* were identified. These genes contain both synonymous and non-synonymous variants that span benign and VUS classifications. Notably, *OR4F21* exhibited two novel VUS (K310R, F44L), indicating possible regulatory functions yet to be fully understood. The observed variation in *LCORL* (L1734P, P1709R), a gene previously associated with growth disorders and Alzheimer's, suggests it may play a broader role in developmental pathways relevant to CTA (Scelsi et al., 2018)(Lin et al., 2017). Similarly, *TNS2* is involved in kidney diseases and cancer (Ashraf et al., 2018)(Cheng et al., 2018), while *VWA8* variants are implicated in kidney diseases, cleft lip and palate, cancer, and autism, suggesting cross-system genetic influences that could indirectly impact tooth development. (Aylward et al., 2016)(Anney et al., 2010)(Guo et al., 2023).

The identified variants across genes like *TM4SF20* (autism and Alzheimer's) (Krgovic et al., 2022)(Floudas et al., 2014)(Laskowski et al., 2018), *MYH6* (CHD) (Granados-Riveron et al., 2010), and *KNLI* (microcephaly, Cancer) (Genin et al., 2012)(He et al., 2023) highlight potential genetic contributors to systemic or developmental abnormalities, emphasizing the pleiotropic nature of CTA. The presence of two consistently observed variants, *OR4F21* (K310R) and *MRTFB* (A135), highlights genetic diversity across the six CTA cohort. Notably, the *MRTFB* variant has been associated with autism and CHD (Holt et al., 2010), supporting its relevance in neurodevelopmental and cardiovascular disorders. In contrast, *OR4F21* (K310R) has not yet been linked to any specific disease, suggesting it may represent a unique, potentially VUS variant within this cohort. Further investigation could clarify *OR4F21's* role, if any, in



developmental anomalies or other conditions. These findings highlight the importance of exploring shared genetic factors across these conditions, which may contribute to the comorbidity and varied clinical presentations observed in patients. Pathway enrichment analysis of the WES panel demonstrated significant roles in DNA damage response, cell cycle regulation, and apoptotic signaling pathways, all critical to cellular stability and development. The involvement of biological processes like DNA replication and repair aligns with the rapid cell division and differentiation required during early tooth bud formation. Additionally, enriched cellular components, including mitochondrial complexes and cell junctions, imply a substantial role for these genes in energy metabolism, cell communication, and genomic stability—all essential for normal tooth development (Sui et al., 2023)(Nijakowski et al., 2023). The R158Q variant in the *LOX* is classified as benign, with a frequency of 17.02%, suggesting evolutionary neutrality. This c.473G>A nucleotide change leads to a non-synonymous coding mutation that does not impair LOX function. As a top 10 hub gene, LOX plays a critical role in collagen and elastin cross-linking, maintaining extracellular matrix stability. Although benign, the variant's presence in three patient samples, highlights its relevance and possible involvement in pathways associated with cancer, diabetes, and heart conditions. Further studies could explore any subtle phenotypic effects associated with its prevalence.

PPI network analysis revealed a well-connected structure with 470 nodes and 1211 interactions, including 11 network modules and key hub genes such as *TNF*, *TP53*, *STAT3*, and *CXCL12*. The clustering of developmental genes within the network suggests their relevance in tooth morphogenesis, with central genes like *TP53* and *STAT3* indicating their involvement in cellular proliferation and apoptosis, both critical to the formation and patterning of teeth (Romano et al., 2012)(Yamashiro et al., 2022). The network's connectivity metrics, with an average of 5.153 neighbors per node and a clustering coefficient of 0.126, underscore the strong interactions between these candidate genes, emphasizing their potential coordinated role in CTA pathogenesis.

The multi-omics integration analysis, combining data from the WES panel and GSE56486 datasets, highlights several shared genes and pathways potentially involved in CTA. By identifying gene overlaps across WES Panel, GSE56486\_UP, and GSE56486\_Down datasets, this approach underscores both unique and shared molecular signatures in CTA. The integration revealed 18 common genes between WES and upregulated GSE56486 genes, and 15 between WES and downregulated GSE56486 genes, suggesting functional or regulatory relationships that may influence dental development.

Pathway enrichment of upregulated genes identified associations with NOD-like receptor signaling, steroid biosynthesis, and cytoskeletal metabolism. These pathways have well-established roles in immune response regulation, cellular signaling, and structural stability, suggesting that dysregulation could impact the ectodermal tissues involved in tooth formation (Lopez-Pajares et al., 2013). Conversely, downregulated genes were linked to pathways like endocytosis, bacterial invasion of epithelial cells, and fatty acid degradation, hinting at compromised metabolic activities that could indirectly influence cellular processes essential for tooth morphogenesis.

The functional analysis further emphasized that upregulated genes are primarily associated with binding activities, enzymatic functions, and extracellular matrix formation, which are essential for tissue adhesion and structural integrity during tooth development (Nowwarote et al., 2022). Downregulated genes, meanwhile, are involved in oxidoreductase activities, cytoskeletal binding, and ion transport—processes critical for cellular organization and signaling. Notably, downregulated genes' involvement in cell junctions and cytoskeleton components may indicate disrupted cellular cohesion or communication in CTA, potentially affecting morphogenesis and cellular architecture.

Among the 33 differentially expressed genes (DEGs), notable variants were identified. *ENAH*, which displayed a benign deletion variant (ERQERLD217D) in multiple samples, is known for its role in actin dynamics and cell motility, which are crucial during morphogenesis (Hwang et al., 2022). Additionally, *LOX* (R158Q), with a benign non-synonymous variant, is involved in extracellular matrix stabilization, further supporting the role of structural integrity in CTA. Several genes, including *IRF5*, *CEL*, and *ABTB2*, presented VUS, adding potential regulatory or structural effects that could contribute to variability in phenotypes. Moreover, benign and VUS variants in genes like *RNF175*, *TGFB1*, and *PRKCB*—which play roles in immune signaling and tissue remodeling—suggest genetic factors that may influence disease progression and severity.

The mutaRNA analysis reveals significant variations in the structural impacts of single nucleotide changes in RNA snippets of the examined genes. Utilizing remuRNA's computed relative entropy scores ( $H(\text{wt}:\text{mu})$ ), we assess how specific SNPs perturb local RNA structures, with higher scores indicating greater alterations. The *WNT10A* c.403G>T variant stands out with a relative entropy score of 3.409, suggesting substantial structural changes, while *EDA* c.467G>A (2.248) and *TSPEAR* c.656T>C (1.392) also indicate notable impacts. In contrast, *WNT10A* c.433G>A shows a lower score of 0.355, indicating a lesser effect on RNA structure.

Base pairing probabilities and accessibility profiles further elucidate these structural consequences (Figures 1, 2, 3). The pronounced alterations in base pairing, particularly for *WNT10A* c.403G>T and *TSPEAR* c.656T>C, suggest disruptions in RNA folding that may affect function and stability. Although *WNT10A* c.433G>A and *EDA* c.467G>A exhibit only minor structural changes, even slight variations can influence RNA-protein interactions, which are crucial for genes like *WNT10A*, involved in development and tissue homeostasis.

Overall, these findings highlight the necessity of considering RNA accessibility alongside structural features to fully understand the functional consequences of genetic variants. This research underscores the importance of further experimental validation and functional assays to clarify the precise effects of these variants on RNA structure and function, providing insights into the molecular mechanisms related to disease pathogenesis or specific cellular phenotypes (Salari et al., 2013).

The evolutionary conservation and protein structure analyses reveal critical insights into how specific gene variants impact protein stability and function, underscoring their potential roles in CTA. The conservation analysis highlighted highly conserved variants, such as *TSPEAR L219P*, *WNT10A A135S*, *WNT10A V145M*, and *EDA R156H*, with conservation scores of 9 out of 9. This strong conservation suggests that these amino acids play essential roles in protein function, where mutations are likely to have significant biological consequences. The slight decrease in conservation for *TSPEAR L219P* (score of 8) still indicates considerable functional importance, while the truncating mutations in *PAX9 Q145* and *TSPEAR I419fs150* remove highly conserved regions, further supporting their likely disruptive impact.

The structural stability analysis across multiple predictive tools identified *TSPEAR L219P*, *WNT10A A135S*, *WNT10A V145M*, and *EDA R156H* as predominantly destabilizing, suggesting a decrease in protein stability. These destabilizing effects, indicated by negative  $\Delta\Delta G$  values, imply structural changes that could impair protein function, especially in *TSPEAR L219P* with  $\Delta\Delta G$  values as low as -5.93 kcal/mol. For *WNT10A A135S*, a consistent destabilization was observed across models, particularly in DUET (-2.606 kcal/mol). Mixed predictions for *WNT10A V145M* suggest that some aspects of the protein structure may tolerate the mutation, although overall stability is likely reduced. In contrast, *EDA R156H* shows a modest destabilizing trend with  $\Delta\Delta G$  of -1.20 kcal/mol, hinting at a minor impact on stability that may still influence biological function. Truncating variants like *PAX9 Q145* and *TSPEAR I419fs150*

were not evaluated for stability due to their nature but are presumed to have severe functional impacts due to significant protein loss.

The tertiary structure analysis of these gene variants revealed marked structural changes in proteins with non-synonymous variants. For instance, *WNT10A* variants (A135S and V145M) demonstrated alterations in helices and strands, potentially affecting protein folding and function. The structural analysis of *TSPEAR* variants (L219P and I419fs\*150) identified disruptions in transmembrane helices and signal peptides, likely influencing protein localization and cell signaling capabilities. These structural disturbances in *TSPEAR* could impair its function in ectodermal tissue development, relevant to CTA pathogenesis. Additionally, *EDA*'s R156H variant was associated with altered metal-binding and extracellular domains, suggesting potential changes in the protein's extracellular signaling function, critical for ectodermal organ development(Bohring et al., 2009).

Protein disorder predictions further support the destabilizing nature of these variants, with disorder profile changes in the *WNT10A*, *TSPEAR*, and *EDA* genes indicating altered flexibility in mutant forms. Both *WNT10A* variants (A135S, V145M) showed shifts in disordered regions, which could impact protein stability and interactions. The frameshift in *TSPEAR* (I419fs\*150) notably shifts disorder profiles, while the *EDA* R156H variant exhibits altered disorder segments, potentially modifying extracellular interactions in pathways crucial for tooth development. The post-translational modifications (PTMs) observed in proteins linked to tooth development, including *WNT10A*, *TSPEAR*, *EDA*, and *PAX9*, reveal diverse impacts on cellular functions such as protein stability, signaling, and chromosome maintenance (Audagnotto & Dal Peraro, 2017). These mutations affect critical pathways involved in cellular homeostasis and developmental processes essential for tooth formation. The distinct roles of each variant underscore how specific PTM changes can contribute to dental abnormalities, highlighting potential targets for therapeutic intervention in congenital tooth defects. This analysis enhances our understanding of PTM-driven mechanisms in tooth morphogenesis and could inform future strategies in dental tissue engineering.

GO enrichment analysis of these variants relative to wild-type forms showed alterations in biological processes, molecular functions, and cellular components, suggesting that these variants influence protein roles in critical pathways. *WNT10A* variants displayed reduced hydrophobicity, while *PAX9 Q145* exhibited increased hydrophobicity, indicating altered structural properties that may affect protein folding and stability. *TSPEAR* compound

heterozygous variants showed variable changes in hydrophobicity, while *EDA R156H* demonstrated a notable increase, which could alter protein conformation and interactions within the cellular environment.

The molecular dynamics (MD) simulations provide a detailed assessment of the structural stability, flexibility, and biophysical properties of protein variants linked to CTA. Over a 10 ns simulation period, proteins reached equilibrium, enabling an analysis of their structural deviations and interactions. Root Mean Square Deviation (RMSD) values indicate that the *EDA\_R156H* variant experiences the highest deviation (3.073 Å), suggesting considerable structural instability. In contrast, *WNT10A\_WT* remains highly stable, with an RMSD of just 0.128 Å, reflecting the stability of this protein's wild-type conformation. RMSF values reveal that *EDA\_R156H* and *TSPEAR\_Compound\_Hetero* display the highest flexibility, at 1.106 Å and 0.675 Å, respectively, potentially disrupting specific interactions or affecting protein function critical to signaling pathways in tooth formation. The SAS values show that *EDA\_R156H* has a markedly increased surface area (124.049 Å<sup>2</sup>), which could indicate partial unfolding, thereby altering interactions with other proteins or ligands. Hydrogen bond counts are notably lower in *EDA* and *TSPEAR* variants; *TSPEAR\_Compound\_Hetero*, for example, has only 250.722 H-bonds compared to *TSPEAR\_WT* with 421.84, suggesting reduced intramolecular stability due to mutations. The Radius of Gyration (Rg) data reveals that *TSPEAR\_Compound\_Hetero* has the highest Rg value (2.349 Å), indicating an expanded structure that may impact the protein's stability and localization. Structural expansion, especially in proteins with signaling functions, could affect their proper localization and interactions within ectodermal tissues relevant to dental development. PCA results offer a comparative view of the biophysical characteristics of these variants. *WNT10A* wild-type and its variants (V145M, A135S) cluster closely, suggesting minimal structural alteration. Conversely, *TSPEAR* variants, including *TSPEAR\_419fs150* and *TSPEAR+Compound Hetero*, are distinctly separated from *TSPEAR\_WT*, highlighting significant structural changes. Notably, the *EDA\_R156H* variant showed substantial dispersion from its wild type, reinforcing its likely structural or functional impact in CTA.

## 5. Conclusion

This study reveals key genetic variants associated with CTA through WES and multi-omics integration. It significantly enhances our understanding of the genetic underpinnings of CTA by

uncovering both novel and established variants in crucial genes involved in tooth development. The integrative multi-omics analysis reveals the intricate nature of CTA and underscores the power of these approaches in dissecting its complex genetic landscape. Key genes such as *WNT10A*, *EDA*, *PAX9*, and *TSPEAR* have emerged as central contributors to the pathogenesis of tooth agenesis, offering valuable insights for future functional investigations. Disruption in critical signaling pathways, including WNT and EDA, plays a significant role in tooth development, as revealed by functional analyses. Additionally, in silico functional and structural predictions provide further support for their involvement in the underlying mechanisms of tooth agenesis, paving the way for deeper exploration in future research. The identified genetic variants also show associations with a range of systemic conditions, including AZ, ALS, autism, CHD, nephropathy, cleft lip palate, COVID-19, and cancer. For instance, *TM4SF20* is linked to AZ and autism, while *LCORL* is implicated in growth disorders and AZ. *TNS2* is associated with kidney diseases, and *MYH6* with CHD. Additionally, *VWA8* is connected to both COVID-19 and autism, and *MRTFB* is involved in both autism and CHD. These findings suggest potential shared genetic pathways between tooth agenesis and various systemic conditions. Moving forward, further research is essential to validate the identified VUS and explore their functional roles in developmental signaling pathways, which could ultimately inform therapeutic strategies for CTA and related disorders.

## 6. Acknowledgement

We gratefully acknowledge the Indian Council of Medical Research (ICMR) for providing the Senior Research Fellowship (SRF) to PR and CD.

## 7. Author Contribution

**PR** conceived the research idea, conducted experiments, performed bioinformatics and data analysis, and wrote the manuscript. **CD** contributed to data analysis. **NV** was responsible for identifying CTA patients and conducting OPG analysis. **RB** and **VKS** carried out clinical investigations. **PD** co-conceived the research idea and approval of final draft.

## 8. Declaration

**Competing interests:** The authors declare no conflict of interest.

**Consent to participate:** All subjects participating in this study were fully informed about the purpose, process, potential risks and benefits of the study and voluntarily signed a written informed consent form.

**Human ethics: Ref No: I.Sc./ECM-XII/2021-2024:** The research protocol received approval from the Ethics Committee of the Institute of Science, Banaras Hindu University, UP, Varanasi, India.

**Funding:** There was no funding for this project.

**Data availability:** The data supporting this study can be made available upon request.

## 9. References

- Adzhubei, I., & Jordan, D. M. (n.d.). Sunyaev, predicting functional effect of human missense mutations using PolyPhen-2. *Curr Protoc Hum Genet*, 7.
- Anney, R., Klei, L., Pinto, D., Regan, R., Conroy, J., Magalhaes, T. R., Correia, C., Abrahams, B. S., Sykes, N., & Pagnamenta, A. T. (2010). A genome-wide scan for common alleles affecting risk for autism. *Human Molecular Genetics*, 19(20), 4072–4082.
- Ashraf, S., Kudo, H., Rao, J., Kikuchi, A., Widmeier, E., Lawson, J. A., Tan, W., Hermle, T., Warejko, J. K., & Shril, S. (2018). Mutations in six nephrosis genes delineate a pathogenic pathway amenable to treatment. *Nature Communications*, 9(1), 1960.
- Audagnotto, M., & Dal Peraro, M. (2017). Protein post-translational modifications: In silico prediction tools and molecular modeling. *Computational and Structural Biotechnology Journal*, 15, 307–319.
- Aylward, A., Cai, Y., Lee, A., Blue, E., Rabinowitz, D., Haddad Jr, J., & Genomics, U. of W. C. for M. (2016). Using whole exome sequencing to identify candidate genes with rare variants in nonsyndromic cleft lip and palate. *Genetic Epidemiology*, 40(5), 432–441.
- Bauer, R. A., Bourne, P. E., Formella, A., Frömmel, C., Gille, C., Goede, A., Guerler, A., Hoppe, A., Knapp, E.-W., & Pöschel, T. (2008). Superimpose: a 3D structural superposition server. *Nucleic Acids Research*, 36(suppl\_2), W47–W54.
- Bellaousov, S., Reuter, J. S., Seetin, M. G., & Mathews, D. H. (2013). RNAstructure: web servers for RNA secondary structure prediction and analysis. *Nucleic Acids Research*, 41(W1), W471–W474.
- Berendsen, H. J. C., van der Spoel, D., & van Drunen, R. (1995). GROMACS: A message-

- passing parallel molecular dynamics implementation. *Computer Physics Communications*, 91(1–3), 43–56.
- Berk, K. N., & Carey, P. (1998). *Data Analysis with Microsoft Excel*. Duxbury Press Pacific Grove, CA.
- Bernhart, S. H., Mückstein, U., & Hofacker, I. L. (2011). RNA Accessibility in cubic time. *Algorithms for Molecular Biology*, 6, 1–7.
- Blom, N., Gammeltoft, S., & Brunak, S. (1999). Sequence and structure-based prediction of eukaryotic protein phosphorylation sites. *Journal of Molecular Biology*, 294(5), 1351–1362.
- Bohring, A., Stamm, T., Spaich, C., Haase, C., Spree, K., Hehr, U., Hoffmann, M., Ledig, S., Sel, S., & Wieacker, P. (2009). WNT10A mutations are a frequent cause of a broad spectrum of ectodermal dysplasias with sex-biased manifestation pattern in heterozygotes. *The American Journal of Human Genetics*, 85(1), 97–105.
- Bonczek, O., Balcar, V. J., & Šerý, O. (2017). PAX9 gene mutations and tooth agenesis: A review. *Clinical Genetics*, 92(5), 467–476.
- Buchan, D. W. A., & Jones, D. T. (2019). The PSIPRED protein analysis workbench: 20 years on. *Nucleic Acids Research*, 47(W1), W402–W407.
- Capriotti, E., Fariselli, P., & Casadio, R. (2005). I-Mutant2. 0: predicting stability changes upon mutation from the protein sequence or structure. *Nucleic Acids Research*, 33(suppl\_2), W306–W310.
- Cardoso, J., Carvalho, D., & Silva, C. C. (2021). Hypohidrotic ectodermal dysplasia and its manifestations in the oral cavity. *J Dent Oral Disord*, 7, 1161.
- Chen, C., Chen, H., Zhang, Y., Thomas, H. R., Frank, M. H., He, Y., & Xia, R. (2020). TBtools: an integrative toolkit developed for interactive analyses of big biological data. *Molecular Plant*, 13(8), 1194–1202.
- Chen, E. Y., Tan, C. M., Kou, Y., Duan, Q., Wang, Z., Meirelles, G. V., Clark, N. R., & Ma'ayan, A. (2013). Enrichr: interactive and collaborative HTML5 gene list enrichment analysis tool. *BMC Bioinformatics*, 14, 1–14.
- Cheng, L.-C., Chen, Y.-L., Cheng, A.-N., Lee, A. Y.-L., Cho, C.-Y., Huang, J.-S., & Chuang, S.-E. (2018). AXL phosphorylates and up-regulates TNS2 and its implications in IRS-1-associated metabolism in cancer cells. *Journal of Biomedical Science*, 25, 1–13.
- Chin, C.-H., Chen, S.-H., Wu, H.-H., Ho, C.-W., Ko, M.-T., & Lin, C.-Y. (2014). cytoHubba: identifying hub objects and sub-networks from complex interactome. *BMC Systems Biology*, 8, 1–7.
- Cowan, R., & Grosdidier, G. (2000). Visualization tools for monitoring and evaluation of distributed computing systems. *Proc. of the International Conference on Computing in High Energy and Nuclear Physics, Padova, Italy*.
- Deng, W., Wang, C., Zhang, Y., Xu, Y., Zhang, S., Liu, Z., & Xue, Y. (2016). GPS-PAIL: prediction of lysine acetyltransferase-specific modification sites from protein sequences. *Scientific Reports*, 6(1), 1–10.
- Devi, C., Ranjan, P., & Das, P. (2024). An integrative analysis of functional consequences of PKD2 missense variants on RNA and protein structures: a computational approach. *Egyptian Journal of Medical Human Genetics*, 25(1), 131.
- Devi, C., Ranjan, P., Raj, S., & Das, P. (2024). Computational Exploration of Protein Structure

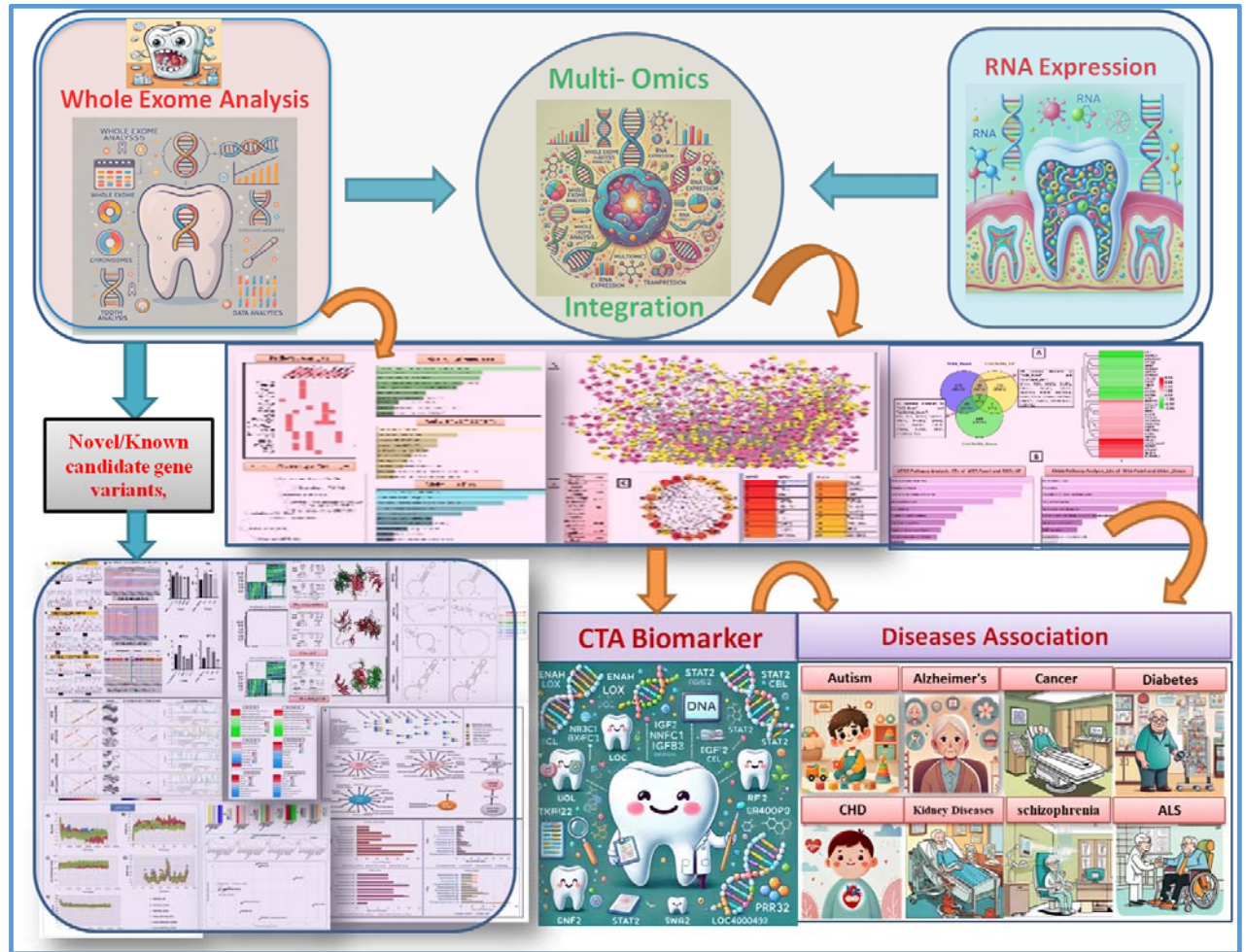


- Dynamics and RNA structural Consequences of PKD1 Missense Variants: Implications in ADPKD Pathogenesis. *BioRxiv*, 2003–2024.
- Doncheva, N. T., Morris, J. H., Gorodkin, J., & Jensen, L. J. (2018). Cytoscape StringApp: network analysis and visualization of proteomics data. *Journal of Proteome Research*, *18*(2), 623–632.
- Du, R., Dinckan, N., Song, X., Coban-Akdemir, Z., Jhangiani, S. N., Guven, Y., Aktoren, O., Kayserili, H., Petty, L. E., & Muzny, D. M. (2018). Identification of likely pathogenic and known variants in TSPEAR, LAMB3, BCOR, and WNT10A in four Turkish families with tooth agenesis. *Human Genetics*, *137*, 689–703.
- Floudas, C. S., Um, N., Kamboh, M. I., Barmada, M. M., & Visweswaran, S. (2014). Identifying genetic interactions associated with late-onset Alzheimer’s disease. *BioData Mining*, *7*, 1–19.
- Galluccio, G., Castellano, M., & La Monaca, C. (2012). Genetic basis of non-syndromic anomalies of human tooth number. *Archives of Oral Biology*, *57*(7), 918–930.
- Gao, Y., Jiang, X., Wei, Z., Long, H., & Lai, W. (2023). The EDA/EDAR/NF- $\kappa$ B pathway in non-syndromic tooth agenesis: A genetic perspective. *Frontiers in Genetics*, *14*, 1168538.
- Genin, A., Desir, J., Lambert, N., Biervliet, M., Van Der Aa, N., Pierquin, G., Killian, A., Tosi, M., Urbina, M., & Lefort, A. (2012). Kinetochores KMN network gene CASC5 mutated in primary microcephaly. *Human Molecular Genetics*, *21*(24), 5306–5317.
- Glaser, F., Pupko, T., Paz, I., Bell, R. E., Bechor-Shental, D., Martz, E., & Ben-Tal, N. (2003). ConSurf: identification of functional regions in proteins by surface-mapping of phylogenetic information. *Bioinformatics*, *19*(1), 163–164.
- Granados-Riveron, J. T., Ghosh, T. K., Pope, M., Bu’Lock, F., Thornborough, C., Eason, J., Kirk, E. P., Fatkin, D., Feneley, M. P., & Harvey, R. P. (2010).  $\alpha$ -Cardiac myosin heavy chain (MYH6) mutations affecting myofibril formation are associated with congenital heart defects. *Human Molecular Genetics*, *19*(20), 4007–4016.
- Guo, M., Li, F., Zhao, L., Fang, Z., Yu, H., Songyang, Z., & Xiong, Y. (2023). Pan-cancer investigation of C-to-U editing reveals its important role in cancer development and new targets for cancer treatment. *Frontiers in Oncology*, *13*, 1097667.
- Hansen, J. E., Lund, O., Tolstrup, N., Gooley, A. A., Williams, K. L., & Brunak, S. (1998). NetOglyc: prediction of mucin type O-glycosylation sites based on sequence context and surface accessibility. *Glycoconjugate Journal*, *15*, 115–130.
- He, K., Li, J., Huang, X., Zhao, W., Wang, K., Wang, T., Chen, J., Wang, Z., Yi, J., & Zhao, S. (2023). KNL1 is a prognostic and diagnostic biomarker related to immune infiltration in patients with uterine corpus endometrial carcinoma. *Frontiers in Oncology*, *13*, 1090779.
- Holt, R., Barnby, G., Maestrini, E., Bacchelli, E., Brocklebank, D., Sousa, I., Mulder, E. J., Kantojärvi, K., Järvelä, I., & Klauck, S. M. (2010). Linkage and candidate gene studies of autism spectrum disorders in European populations. *European Journal of Human Genetics*, *18*(9), 1013–1019.
- Hunter, J., & Dale, D. (2007). The matplotlib user’s guide. *Matplotlib 0.90.0 User’s Guide*.
- Hwang, T., Parker, S. S., Hill, S. M., Grant, R. A., Ilunga, M. W., Sivaraman, V., Mouneimne, G., & Keating, A. E. (2022). Native proline-rich motifs exploit sequence context to target actin-remodeling Ena/VASP protein ENAH. *Elife*, *11*, e70680.
- Jumper, J., Evans, R., Pritzel, A., Green, T., Figurnov, M., Ronneberger, O., Tunyasuvunakool, K., Bates, R., Žídek, A., & Potapenko, A. (2021). Highly accurate protein structure

- prediction with AlphaFold. *Nature*, 596(7873), 583–589.
- Karnik, A., Karnik, R., & Grefen, C. (2013). SDM-Assist software to design site-directed mutagenesis primers introducing “silent” restriction sites. *BMC Bioinformatics*, 14, 1–9.
- Kiefer, F., Arnold, K., Künzli, M., Bordoli, L., & Schwede, T. (2009). The SWISS-MODEL Repository and associated resources. *Nucleic Acids Research*, 37(suppl\_1), D387–D392.
- Kramer, O. (2016). *Machine learning for evolution strategies* (Vol. 20). Springer.
- Krgovic, D., Gorenjak, M., Rihar, N., Opalic, I., Stangler Herodez, S., Gregoric Kumperscak, H., Dovc, P., & Kokalj Vokac, N. (2022). Impaired neurodevelopmental genes in Slovenian autistic children elucidate the comorbidity of autism with other developmental disorders. *Frontiers in Molecular Neuroscience*, 15, 912671.
- Laskowski, R. A., Jabłońska, J., Pravda, L., Vařeková, R. S., & Thornton, J. M. (2018). PDBsum: Structural summaries of PDB entries. *Protein Science*, 27(1), 129–134.
- Lin, Y.-J., Liao, W.-L., Wang, C.-H., Tsai, L.-P., Tang, C.-H., Chen, C.-H., Wu, J.-Y., Liang, W.-M., Hsieh, A.-R., & Cheng, C.-F. (2017). Association of human height-related genetic variants with familial short stature in Han Chinese in Taiwan. *Scientific Reports*, 7(1), 6372.
- Lopez-Pajares, V., Yan, K., Zarnegar, B. J., Jameson, K. L., & Khavari, P. A. (2013). Genetic pathways in disorders of epidermal differentiation. *Trends in Genetics*, 29(1), 31–40.
- Maurer-Stroh, S., & Eisenhaber, F. (2005). Refinement and prediction of protein prenylation motifs. *Genome Biology*, 6(6), 1–15.
- Meade, M. J., & Dreyer, C. W. (2023). Tooth agenesis: an overview of diagnosis, aetiology and management. *Japanese Dental Science Review*, 59, 209–218.
- Miladi, M., Raden, M., Diederichs, S., & Backofen, R. (2020). MutaRNA: analysis and visualization of mutation-induced changes in RNA structure. *Nucleic Acids Research*, 48(W1), W287–W291.
- Nijakowski, K., Ortarzewska, M., Jankowski, J., Lehmann, A., & Surdacka, A. (2023). The role of cellular metabolism in maintaining the function of the dentine-pulp complex: a narrative review. *Metabolites*, 13(4), 520.
- Nowwarote, N., Petit, S., Ferre, F. C., Dingli, F., Laigle, V., Loew, D., Osathanon, T., & Fournier, B. P. J. (2022). Extracellular matrix derived from dental pulp stem cells promotes mineralization. *Frontiers in Bioengineering and Biotechnology*, 9, 740712.
- Oliveros, J. C. (2007). VENNY. An interactive tool for comparing lists with Venn Diagrams. [Http://Bioinfogp.Cnb.Csic.Es/Tools/Venny/Index.Html](http://Bioinfogp.Cnb.Csic.Es/Tools/Venny/Index.Html).
- Parthiban, V., Gromiha, M. M., & Schomburg, D. (2006). CUPSAT: prediction of protein stability upon point mutations. *Nucleic Acids Research*, 34(suppl\_2), W239–W242.
- Peled, A., Sarig, O., Samuelov, L., Bertolini, M., Ziv, L., Weissglas-Volkov, D., Eskin-Schwartz, M., Adase, C. A., Malchin, N., & Bochner, R. (2016). Mutations in TSPEAR, encoding a regulator of notch signaling, affect tooth and hair follicle morphogenesis. *PLoS Genetics*, 12(10), e1006369.
- Pires, D. E. V., Ascher, D. B., & Blundell, T. L. (2014a). DUET: a server for predicting effects of mutations on protein stability using an integrated computational approach. *Nucleic Acids Research*, 42(W1), W314–W319.
- Pires, D. E. V., Ascher, D. B., & Blundell, T. L. (2014b). mCSM: predicting the effects of mutations in proteins using graph-based signatures. *Bioinformatics*, 30(3), 335–342.

- Pugalethi, G., Nithya, V., Chou, K.-C., & Archunan, G. (2020). Nglyc: a random forest method for prediction of N-glycosylation sites in eukaryotic protein sequence. *Protein and Peptide Letters*, 27(3), 178–186.
- Python, W. (2021). Python releases for windows. *Python Releases for Windows*, 24.
- Radivojac, P., Vacic, V., Haynes, C., Cocklin, R. R., Mohan, A., Heyen, J. W., Goebel, M. G., & Iakoucheva, L. M. (2010). Identification, analysis, and prediction of protein ubiquitination sites. *Proteins: Structure, Function, and Bioinformatics*, 78(2), 365–380.
- Ranjan Jr, P., Devi Jr, C., Verma Sr, N., Bansal Sr, R., Srivastava Sr, V. K., & Das Sr, P. (2024). Understanding Tooth Agenesis: A Multi-omics Insight into MicroRNA Regulation. *MedRxiv*, 2009–2024.
- Ranjan, P., & Das, P. (2022). Understanding the impact of missense mutations on the structure and function of the EDA gene in X-linked hypohidrotic ectodermal dysplasia: A bioinformatics approach. *Journal of Cellular Biochemistry*, 123(2), 431–449.
- Ranjan, P., & Das, P. (2023). An inclusive study of deleterious missense PAX9 variants using user-friendly tools reveals structural, functional alterations, as well as potential therapeutic targets. *International Journal of Biological Macromolecules*, 233, 123375.
- Rentzsch, P., Witten, D., Cooper, G. M., Shendure, J., & Kircher, M. (2019). CADD: predicting the deleteriousness of variants throughout the human genome. *Nucleic Acids Research*, 47(D1), D886–D894.
- Romano, R. A., Solomon, L. W., & Sinha, S. (2012). Tp63 in oral development, neoplasia, and autoimmunity. *Journal of Dental Research*, 91(2), 125–132.
- Salari, R., Kimchi-Sarfaty, C., Gottesman, M. M., & Przytycka, T. M. (2013). Sensitive measurement of single-nucleotide polymorphism-induced changes of RNA conformation: application to disease studies. *Nucleic Acids Research*, 41(1), 44–53.
- Sarkar, T., Bansal, R., & Das, P. (2014). Whole genome sequencing reveals novel non-synonymous mutation in ectodysplasin A (EDA) associated with non-syndromic X-linked dominant congenital tooth agenesis. *Plos One*, 9(9), e106811.
- Scelsi, M. A., Khan, R. R., Lorenzi, M., Christopher, L., Greicius, M. D., Schott, J. M., Ourselin, S., & Altmann, A. (2018). Genetic study of multimodal imaging Alzheimer's disease progression score implicates novel loci. *Brain*, 141(7), 2167–2180.
- Schmid, N., Eichenberger, A. P., Choutko, A., Riniker, S., Winger, M., Mark, A. E., & Van Gunsteren, W. F. (2011). Definition and testing of the GROMOS force-field versions 54A7 and 54B7. *European Biophysics Journal*, 40, 843–856.
- Schonberger, S., Kadry, R., Shapira, Y., & Finkelstein, T. (2023). Permanent tooth agenesis and associated dental anomalies among Orthodontically treated children. *Children*, 10(3), 596.
- Schwarz, J. M., Rödelberger, C., Schuelke, M., & Seelow, D. (2010). MutationTaster evaluates disease-causing potential of sequence alterations. *Nature Methods*, 7(8), 575–576.
- Sui, B.-D., Zheng, C.-X., Zhao, W.-M., Xuan, K., Li, B., & Jin, Y. (2023). Mesenchymal condensation in tooth development and regeneration: a focus on translational aspects of organogenesis. *Physiological Reviews*, 103(3), 1899–1964.
- Swift, M. L. (1997). GraphPad prism, data analysis, and scientific graphing. *Journal of Chemical Information and Computer Sciences*, 37(2), 411–412.
- Systèmes, D. (2016). Biovia, discovery studio modeling environment. *Dassault Systèmes Biovia: San Diego, CA, USA*.

- Szklarczyk, D., Franceschini, A., Kuhn, M., Simonovic, M., Roth, A., Minguéz, P., Doerks, T., Stark, M., Muller, J., & Bork, P. (2010). The STRING database in 2011: functional interaction networks of proteins, globally integrated and scored. *Nucleic Acids Research*, *39*(suppl\_1), D561–D568.
- Thumuluri, V., Almagro Armenteros, J. J., Johansen, A. R., Nielsen, H., & Winther, O. (2022). DeepLoc 2.0: multi-label subcellular localization prediction using protein language models. *Nucleic Acids Research*, *50*(W1), W228–W234.
- van den Boogaard, M.-J., Créton, M., Bronkhorst, Y., van der Hout, A., Hennekam, E., Lindhout, D., Cune, M., & van Amstel, H. K. P. (2012). Mutations in WNT10A are present in more than half of isolated hypodontia cases. *Journal of Medical Genetics*, *49*(5), 327–331.
- Vaser, R., Adusumalli, S., Leng, S. N., Sikic, M., & Ng, P. C. (2016). SIFT missense predictions for genomes. *Nature Protocols*, *11*(1), 1–9.
- Worth, C. L., Preissner, R., & Blundell, T. L. (2011). SDM—a server for predicting effects of mutations on protein stability and malfunction. *Nucleic Acids Research*, *39*(suppl\_2), W215–W222.
- Xue, Y., Liu, Z., Gao, X., Jin, C., Wen, L., Yao, X., & Ren, J. (2010). GPS-SNO: computational prediction of protein S-nitrosylation sites with a modified GPS algorithm. *PloS One*, *5*(6), e11290.
- Yamashiro, T., Kurosaka, H., & Inubush, T. (2022). The association between runx signaling and craniofacial development and disease. *Current Osteoporosis Reports*, 1–7.
- Yu, M., Wong, S., Han, D., & Cai, T. (2019). Genetic analysis: Wnt and other pathways in nonsyndromic tooth agenesis. *Oral Diseases*, *25*(3), 646–651.
- Zhao, Q., Xie, Y., Zheng, Y., Jiang, S., Liu, W., Mu, W., Liu, Z., Zhao, Y., Xue, Y., & Ren, J. (2014). GPS-SUMO: a tool for the prediction of sumoylation sites and SUMO-interaction motifs. *Nucleic Acids Research*, *42*(W1), W325–W330.



**Graphical Abstract**

**Table1: Screening of Known and Novel Variations in Candidate Genes in CTA Patients.**

Gene	Location	Variation	Zygoty	Classification	Disease	Inheritance	Known/Novel
------	----------	-----------	--------	----------------	---------	-------------	-------------

(Transcript)		ACMG					
<i>WNT10A</i>	Chr2	V145M c.433G>A	homo	Likely Pathogenic	Tooth Agenesis	AR	Known
<i>EDA</i>	X	R156H, c.467G>A	homo	Likely Pathogenic	Ectodermal Dysplasia	XLR	Known
<i>WNT10A</i>	Chr2	A135S;c.403G>T	hetro	VUS	Tooth Agenesis	AD	Novel
<i>TSPEAR</i>	Chr21	L219P; c.656T>C	hetro	VUS	Tooth Agenesis	AR	Novel
<i>TSPEAR</i>	Chr21	I419Lfs*150: c.1255delA	hetro	VUS	Tooth Agenesis	AR	known
<i>PAX9</i>	Chr14	Stop Gained c.433 C>T; p.Gln 145*	hetro	Pathogenic	Tooth Agenesis	AR	Known

**Note:** VUS: Variant of Uncertain Significance, AD: Autosomal Dominant, AR: Autosomal Recessive.

**Table2. Analysis of Gene Variants Across Databases and Prediction Tools.**

Variants	Database reports					Predictions (scores)				
	1000 genome s	EXA C	gnomAD	Turkish Variome	OMIM	ClinVar	SIFT	Polyphen-2	Mutatio nTaster 2	CADD3 Phred score
<i>TSPEAR</i> : L219P;c.656T>C	NA	NA	NA	NA	603140	NA	NA	NA	NA	26
<i>TSPEAR</i> : I419fs*150 : c.1255delA	NA	<0.01	<0.01	NA	603140	NA	NA	NA	D	NA
<i>PAX9</i> : Q145*;c.433C>T	NA	NA	NA	NA	128400	NA	D	D	D	D
<i>WNT10A</i> :A135S; c.403G>T	NA	NA	NA	NA	608522	NA	D	D	D	24.4
<i>WNT10A</i> (V145M) c.433G>A	NA	0.0025	0.0073	0.0446%	606268	Likely Pathogenic	D	D	D	25.1
<i>EDA</i> : p.R156H; c.467G>A	NA	NA	0.0009	0.0356	129920	NA	D	D	D	26.8

**Notes:** This table summarizes variant details, including relevant database reports and pathogenicity predictions. "NA" signifies data unavailability. The prediction scores indicate potential impacts on protein function: "D" denotes a damaging prediction by SIFT, PolyPhen-2, and MutationTaster2, while the CADD3 Phred score highlights variants with higher pathogenic potential, generally above 20.

**Table 3: Analysis of genes identified across all six tooth agenesis patients, highlighting the presence of different variants within each gene.**

Gene	Function/Diseases	VARIANT/AA Position	ACMG	MAF/NOVEL	HGVSC	Effect	Samples Present
<b>TM4SF20</b>	Tetraspanin, cell adhesion/ <b>Autism, AZ</b>	A27V	Benign	10.68%	c.80C>T	NON_SYNONYMOUS_CODING	DEN1, DEN10, DEN20, DEN12
<b>LCORL</b>	Transcriptional regulator/ <b>Growth Dev., AZ</b>	L1734P	VUS	<b>Novel</b>	c.5201T>C	NON_SYNONYMOUS_CODING	DEN1
<b>LCORL</b>	Transcriptional regulator/ <b>Growth Dev., AZ</b>	P1709R	VUS	<0.01%	c.5126C>G	NON_SYNONYMOUS_CODING	DEN1
<b>LCORL</b>	Transcriptional regulator/ <b>Growth Dev., AZ</b>	T1042	Benign	13.14%	c.3126T>C	SYNONYMOUS_CODING	DEN10, DEN20.1, DEN24.1, DEN12
<b>OR4F21</b>	Olfactory receptor/ <b>No diseases reported</b>	K310R	VUS	<b>Novel</b>	c.929A>G	NON_SYNONYMOUS_CODING	DEN1, DEN10, DEN20.1, DEN24.1, DEN12, DEN23.1
<b>OR4F21</b>	Olfactory receptor/ <b>No diseases reported</b>	F44L	VUS	<b>Novel</b>	c.130T>C	NON_SYNONYMOUS_CODING	DEN1, DEN20.1, DEN12
<b>TNS2</b>	Tensin protein, cell migration/ <b>Kidney Diseases</b>	I858M	VUS	0.02%	c.2574C>G	NON_SYNONYMOUS_CODING	DEN1
<b>TNS2</b>	Tensin protein, cell migration/ <b>Kidney Diseases</b>	G774E	Benign	0.11%	c.2321G>A	NON_SYNONYMOUS_CODING	DEN12

<b>VWA8</b>	Von Willebrand factor type A domain/ <b>Covid19, Cleft Lip Palate, Autism</b>	R552H	Benign	5.53%	c.1655G>A	NON_SYNONYMOUS_CODING	DEN1
<b>VWA8</b>	Von Willebrand factor type A domain/ <b>Covid19, Cleft Lip Palate, Autism</b>	I1439L	Benign	1.44%	c.4315A>C	NON_SYNONYMOUS_CODING	DEN10
<b>MYH6</b>	Myosin heavy chain, cardiac muscle/ <b>CHD</b>	G56R	Benign	7.83%	c.166G>A	NON_SYNONYMOUS_CODING	DEN10, DEN12
<b>KNL1</b>	Kinetochores protein/ <b>Mic rocephaly, Cancer</b>	A1270V	VUS	0.01%	c.3809C>T	NON_SYNONYMOUS_CODING	DEN20.1
<b>LOC400499</b>	Hypothetical protein/ <b>Unknown</b>	G2806R	NA	NA	c.8416G>A	NON_SYNONYMOUS_CODING	DEN1
<b>LOC400499</b>	Hypothetical protein/ <b>Unknown</b>	I176V	NA	NA	c.526A>G	NON_SYNONYMOUS_CODING	DEN20.1
<b>MRTFB</b>	Myocardin-related transcription factor/ <b>Autism, CHD</b>	A135	Benign	7.88%	c.405T>C	SYNONYMOUS_CODING	DEN1, DEN10, DEN20.1, DEN24.1, DEN12, DEN23.1
<b>PRR32</b>	Proline-rich protein/ <b>Intellectual Development Disorder</b>	M193T	Benign	9.89%	c.578T>C	NON_SYNONYMOUS_CODING	DEN20.1, DEN24.1

**Note:** This table presents gene variants, their functions, and disease associations across samples. "VUS" (variant of uncertain significance) requires further study for clinical impact. "NOVEL"



denotes newly observed variants. "Benign" and "NA" Not Available. Highlighted showed present in all samples. To maintain confidentiality and anonymity, each sample was assigned a unique study code.

**Table 4: Comprehensive Analysis of Variants in 33 DEGs Common to the WES Panel and Top 10 Hub Genes.**

Gene	Function/Diseases	AA Change	ACMG	MAF/NOVEL	CTA_DEGs	HGVSC	Effect	Samples
<i>ENAH</i>	Actin polymerization regulator involved in cell motility and morphology/ <b>Cancer, Nephropathy.</b>	ERQER LD217D	Benign	9.59%	UP regulated	c.651_668 delGCGG CAGGAA CGCCTG GA	CODON_CHANGE_PLUS_CODON_DELETION	DEN1, DEN20.1
<i>LOX</i>	Lysyl oxidase; catalyzes the cross-linking of collagen and elastin, crucial for extracellular matrix stability/ <b>Cancer, Diabetic, Heart, ALS</b>	R158Q	Benign	17.02%	NA (Top 10 hub gene)	c.473G>A	NON_SYNONYMOUS_CODING	DEN1, DEN10, DEN20.1
<i>NR3C1</i>	Glucocorticoid receptor; regulates genes controlling development, metabolism, and immune response/ <b>Diabetes, Nephrotic, Crohn Diseases, Heart, Schizophrenia.</b>	N766	Benign	15.02%	UP regulated	c.2298T>C	SYNONYMOUS_CODING	DEN1

<b><i>IRF5</i></b>	Interferon regulatory factor; involved in innate immune response and regulation of inflammatory cytokines/ <b>Auto immune, Bowel, Cancer, Kidney Diseases.</b>	I103V	VUS	<0.01%	Down regulated	c.307A>G	NON_SYNONYMOUS_CODING	DEN1
<b><i>CEL</i></b>	Carboxyl ester lipase; important in the digestion and absorption of dietary fats./ <b>Diabetic, Cancer, Kidney</b>	S654A	VUS	<b>Novel</b>	Down regulated	c.1960T>G	NON_SYNONYMOUS_CODING	DEN1, DEN20.1
<b><i>ABTB2</i></b>	Ankyrin repeat and BTB (POZ) domain-containing protein; associated with cellular signaling pathways/ <b>Cancer.</b>	H250Q	VUS	7.92%	Down regulated	c.750C>G	NON_SYNONYMOUS_CODING	DEN1
<b><i>IGF1</i></b>	Insulin-like growth factor 1; plays a key role in growth and development, especially in muscle and bone/ <b>Cancer, Schizophrenia, Diabetes, Miscarriage.</b>		Benign	9%	NA (Top 10 hub gene)	c.*6433G>C	UTR_3_PRIME	DEN1, DEN10

<b><i>TIMP2</i></b>	Tissue inhibitor of metalloproteinase 2; inhibits matrix metalloproteinases (MMPs), which degrade the extracellular matrix/ <b>Cancer</b> .	S101	Benign	12.54%	NA (Top 10 hub gene)	c.303G>A	SYNONYMOUS_CODING	DEN1, DEN10, DEN20.1
<b><i>RNF175</i></b>	E3 ubiquitin-protein ligase; involved in protein degradation through ubiquitination/ <b>Cancer</b> .	L307F	Benign	18.5%	UP regulated	c.921G>C	NON_SYNONYMOUS_CODING	DEN20.1, DEN24.1, DEN12, DEN23.1
<b><i>TGFB1</i></b>	Transforming growth factor-beta 1; regulates cell proliferation, differentiation, and development, as well as immune responses/ <b>Kidney, Osteosclerosis, Heart, Cancer</b> .	R25P	Benign	7.11%	NA (Top 10 hub gene)	c.74G>C	NON_SYNONYMOUS_CODING	DEN12
<b><i>PRKCB</i></b>	Protein kinase C beta; plays a role in various cellular processes including proliferation, differentiation, and apoptosis/ <b>Diabetes, Cancer</b> .	V139	VUS	<0.01%	UP regulated	c.417G>A	SYNONYMOUS_CODING	DEN10

<b>STAT3</b>	Signal transducer and activator of transcription 3; involved in cell growth and apoptosis regulation, playing a key role in cytokine signalling/ <b>Inflammatory, Autoimmune Diseases.</b>		Benign	7.5%	NA (Top 10 hub gene)	c.*893dup A	UTR_3_PRIME	DEN12
<b>CXCL12</b>	Chemokine (C-X-C motif) ligand 12; mediates chemotaxis, especially involved in immune cell migration and development/ <b>Cancer, Diabetes.</b>		NA	NA	UP regulated	c.*519G> A	UTR_3_PRIME	DEN1, DEN10, DEN12

**Note:** This table includes gene variants, functions, disease associations, and regulatory status across samples. "Benign" indicates non-pathogenicity, while "VUS" (variant of uncertain significance) may require further research. To maintain confidentiality and anonymity, each sample was assigned a unique study code.

**Table 5: Protein Structure Stability Analysis of Gene Variants**

Variants	mCSM Predicted Stability Change ( $\Delta\Delta G$ )	SDM Predicted Stability Change ( $\Delta\Delta G$ )	DUET Predicted Stability Change ( $\Delta\Delta G$ )	CUPSAT	I-Mutant	MUpro
<b>TSPEAR: L219P</b>	-1.284 kcal/mol (Destabilizing)	-4.31 kcal/mol (Destabilizing)	-1.959 kcal/mol (Destabilizing)	(Destabilizing) -5.93 kcal/mol	-1.38 kcal/mol Destabilising	-1.8029236 kcal/mol (DECREASE stability)
<b>TSPEAR:I419fs*150</b>	NA	NA	NA	NA	NA	NA
<b>PAX9: Q145*</b>	NA	NA	NA	NA	NA	NA
<b>WNT10A :A135S</b>	-2.386 kcal/mol (Destabilizing)	-2.57 kcal/mol (Destabilizing)	-2.606 kcal/mol (Destabilizing)	Destabilising -2.92 kcal/mol	-0.07 kcal/mol Destabilising	-0.57849674 kcal/mol (DECREASE stability)
<b>WNT10A: V145M</b>	-1.387 kcal/mol (Destabilizing)	-0.63 kcal/mol (Destabilizing)	-1.454 kcal/mol (Destabilizing)	Stabilising 0.98 kcal/mol	-1.31 kcal/mol Destabilising	-0.69678663 kcal/mol (DECREASE stability)
<b>EDA: R156H</b>	-0.631 kcal/mol (Destabilizing)	0.17 kcal/mol (Stabilizing)	-0.519 kcal/mol (Destabilizing)	Destabilising -0.83	-1.20 kcal/mol Destabilising	-1.5988524 kcal/mol (DECREASE stability)

**Note:** Negative  $\Delta\Delta G$  values indicate destabilizing effects, potentially impacting protein structure. Most tools predict destabilization for variants like TSPEAR: L219P and WNT10A: A135S, with WNT10A: V145M showing mixed results. "NA" denotes unavailable data.

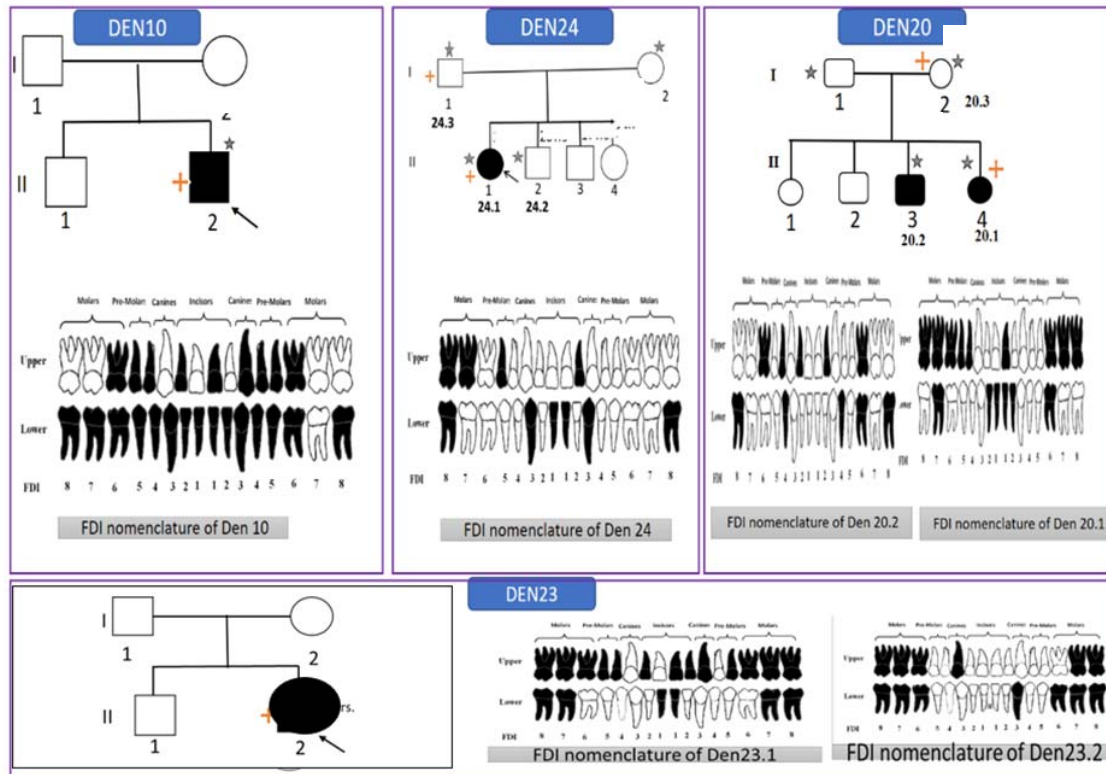


**Figure1: Clinical and Genetic Analysis of Patients with Tooth Agenesis**

Panels (A-D) present clinical and genetic data from patients with tooth agenesis, showing key variants identified in *EDA*, *WNT10A*, *TSPEAR*, and *PAX9* genes: (A) **DEN10**: Pedigree with an *EDA* variant (p.I156H; c.467G>A) and OPG showing dental status. (B) **DEN24**: *WNT10A* variant (p.A135S; c.403G>T) with OPG and FDI dental mapping. (C) **DEN20**: *TSPEAR* variant (p.I219P; c.656T>C) in two family members, with corresponding OPGs. (D) **DEN23**: *PAX9* variant (p.Gln45Ter; c.433C>T) with OPGs for two affected individuals. Each panel includes the patient's pedigree, OPG, and FDI tooth chart to illustrate genotype-phenotype correlations. To maintain confidentiality and anonymity, each sample was assigned a unique study code. Readers are encouraged to contact the corresponding author for access to patients' OPG.

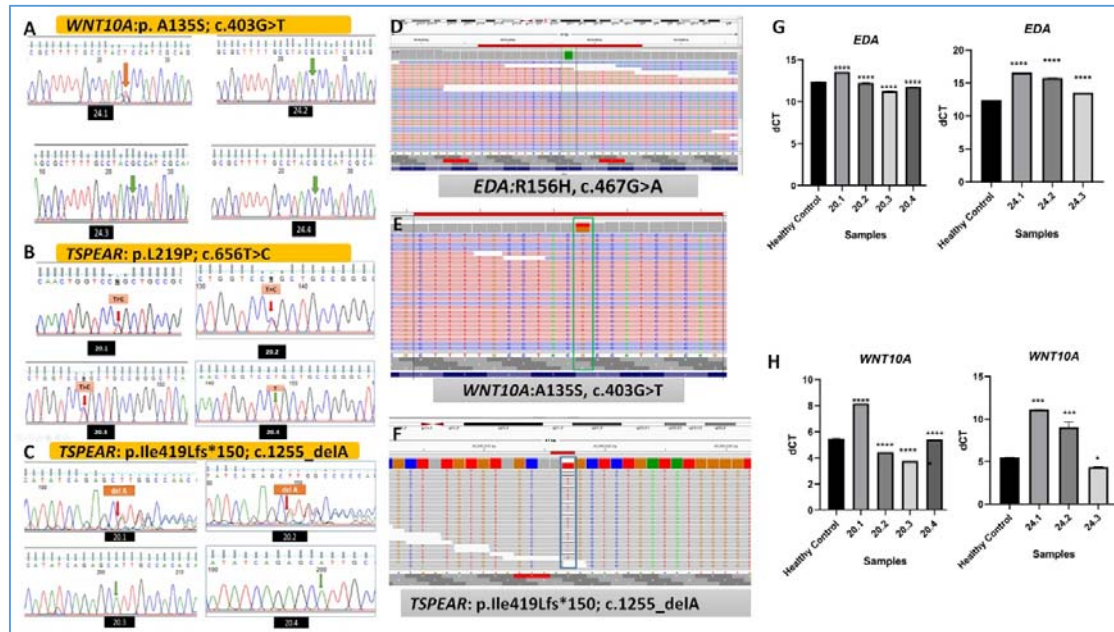


**Figure 2: Validation of genetic variants and their impact on *EDA* and *WNT* signaling through gene expression.**

(A–C) Sanger sequencing chromatograms showing validated variants in the genes *WNT10A* (p.A135S; c.403G>T) (A), *TSPEAR* (p.L219P; c.656T>C) (B), and *TSPEAR* (p.Ile419fs\*150; c.1255\_delA) (C). The red arrows indicate the locations of nucleotide changes, while green arrows show nucleotides that remain unchanged. (D–F) Integrative Genomics Viewer (IGV) screenshots showing the presence of these variants in the sequencing data. Panel (D) shows the *EDA* variant (R156H; c.467G>A), (E) shows the *WNT10A* variant (A135S; c.403G>T), and (F) shows the *TSPEAR* frameshift mutation (p.Ile419fs\*150; c.1255\_delA). (G–H) RT-PCR analysis of *EDA* and *WNT10A* gene expression levels. (G) Relative expression levels of *EDA* in samples carrying the variant compared to the internal control, showing a significant reduction in expression. (H) Relative expression levels of *WNT10A* in samples with the variant, also showing a significant decrease in expression.  $\Delta$ CT values are shown for each sample, with statistical significance indicated as follows: \*\*\*\*p < 0.0001, \*\*\*p < 0.001. These findings indicate that the identified variants affect *EDA* and *WNT* signaling pathways, potentially contributing to the observed phenotypes.

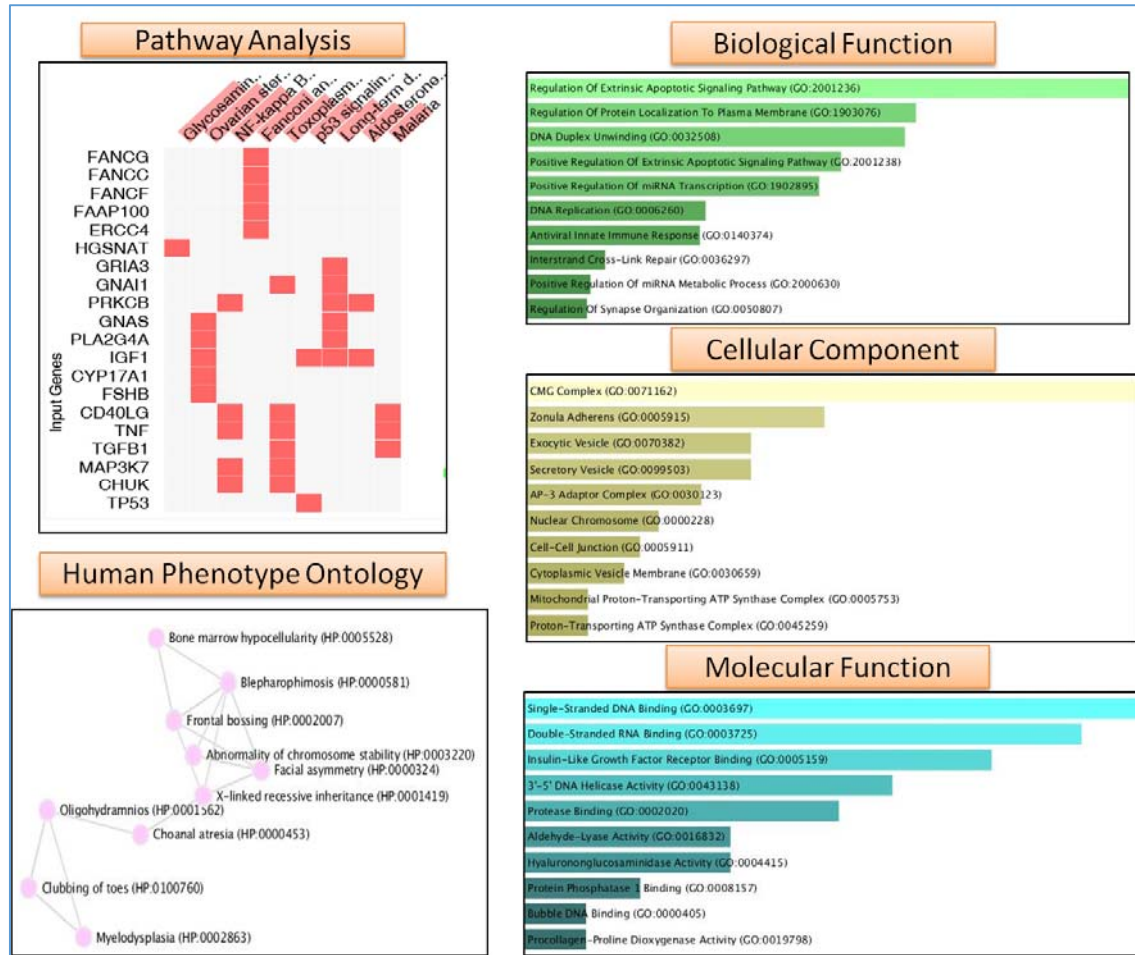


**Figure3: Enrichment analysis of the WES gene panel.** The figure displays the results of enrichment analysis for the identified genes in terms of biological processes, cellular components, and molecular functions. The bars represent the enrichment score for each GO term, indicating the significance of the gene's involvement in the corresponding biological process, cellular component, or molecular function. The results highlight the potential roles of these genes in various cellular pathways and processes.



It is made available under a [CC-BY-NC-ND 4.0 International license](https://creativecommons.org/licenses/by-nc-nd/4.0/).

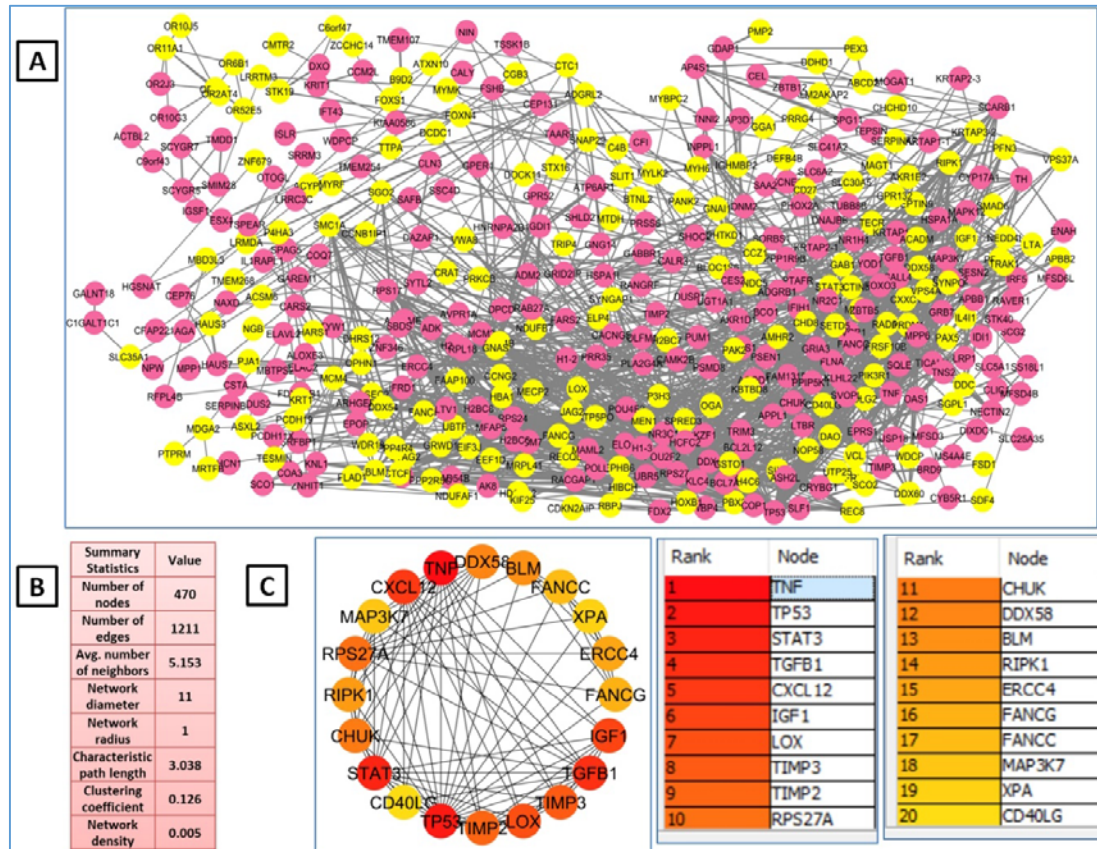


**Figure 4: PPI network analysis of the WES gene panel.** The figure represents the identified genes as nodes connected by edges, indicating protein-protein interactions. Genes involved in developmental processes are highlighted in yellow. The size of each node corresponds to its degree (number of connections), and the color represents its clustering coefficient. The top 20 hub genes (genes with the highest number of connections) are listed in a separate table. **Panel A:** The network visualization, where nodes represent genes and edges represent protein-protein interactions. **Panel B:** Summary statistics of the network, including the number of nodes, edges, average degree, diameter, radius, characteristic path length, clustering coefficient, and network density. **Panel C:** A circular representation of the top 20 hub genes, with their ranks and node names listed. The color gradient indicates the degree of each hub gene.

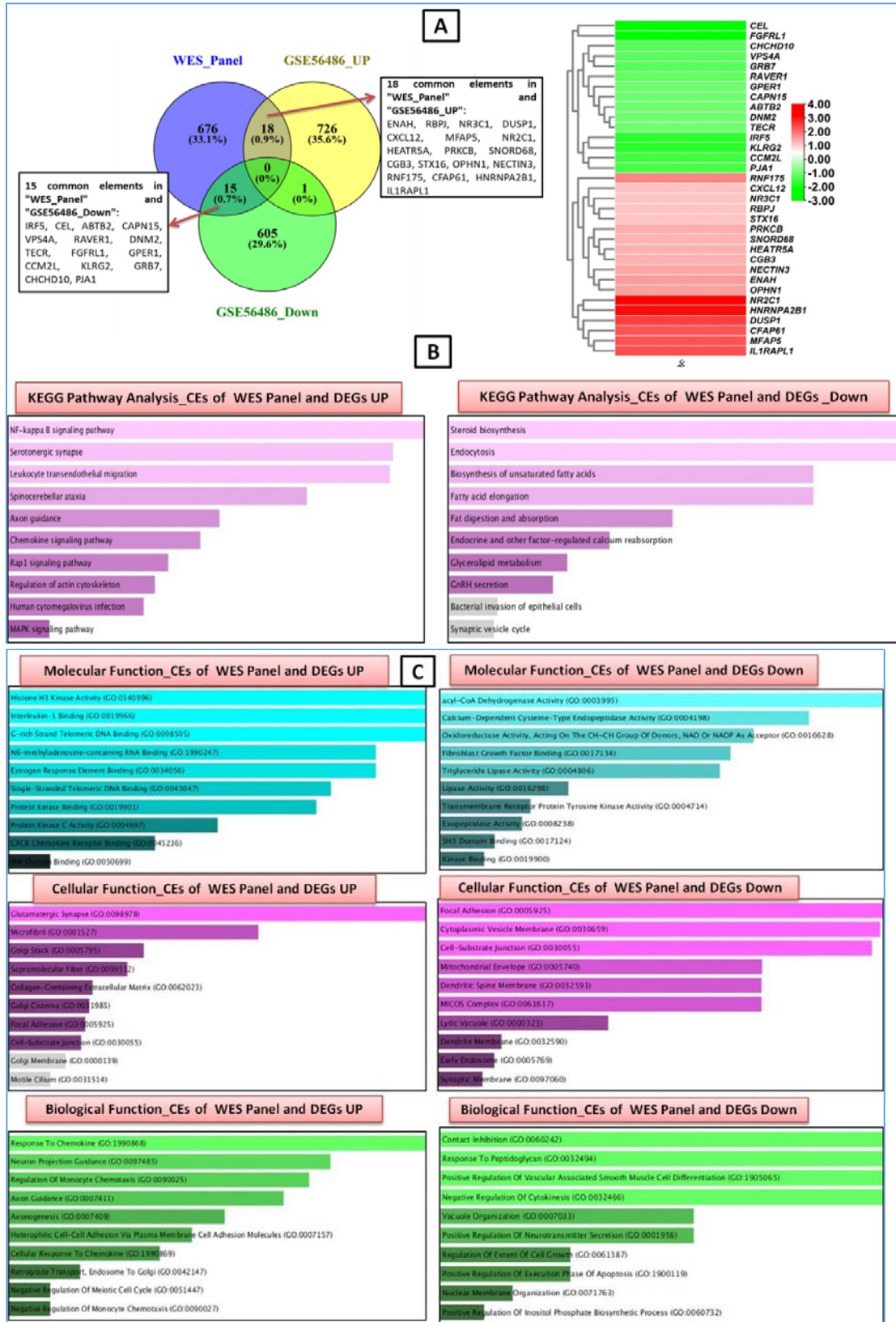


**Figure5: Venn Diagram, Heatmap, Pathway, and GO Enrichment Analysis of Common Elements Between WES Gene Panel and Differentially Expressed Genes (DEGs). Panel A:** A Venn diagram illustrating the intersection between the WES gene panel and DEGs that are upregulated (GSE56486 UP) or downregulated (GSE56486 Down) within the dataset. The numbers in each segment denote the count of genes in each category. Accompanying this, a heatmap visualizes the common elements (CEs) shared between the WES gene panel and DEGs. Color intensity reflects the fold change, with shades of red indicating upregulation and shades of green indicating downregulation. **Panel B:** Pathway analysis of the DEGs, showcasing pathways enriched among the upregulated and downregulated genes. This highlights the pathways significantly affected by gene expression changes within the dataset. **Panel C:** Enrichment analysis of the common elements (CEs) between the WES gene panel and DEGs, showing results for three main Gene Ontology (GO) categories: Biological Processes (BP), Molecular Functions (MF), and Cellular Components (CC). Bars represent the enrichment score for each GO term, indicating the significance of the CEs in the relevant biological processes, molecular functions, or cellular components. This panel underscores the functional distinctions between upregulated and downregulated DEGs within the WES gene panel.

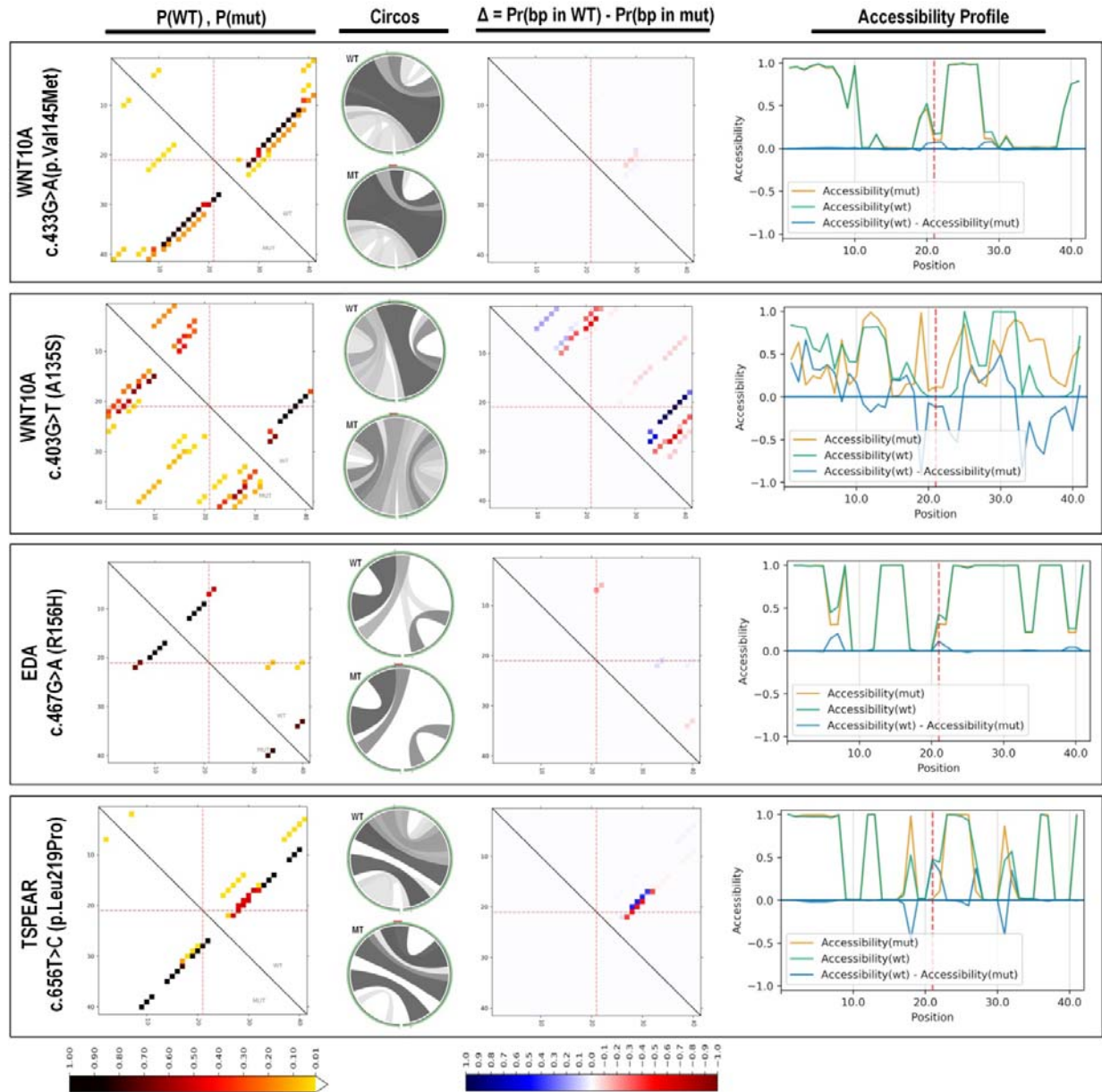


**Figure 6: Analysis of RNA Structural Features.** This figure presents analysis of RNA structural features for both wild type (WT) and mutant (MT) RNA sequences of each variant using mutaRNA tool. The mutated position is indicated by red dotted lines or mark. The first heat map like dot plots with the top-right and bottom-left panels provides a heatmap-like representation of base pairing probabilities in wild-type (p(WT)) and mutant (p(MT)) RNA sequences. The darker dots indicate higher probabilities of base pairing. The upper and lower circos plots visualize the base pair probabilities (p(WT) and p(MT)), with the sequence beginning from the 5' end positioned at the bottom slight-left and extending clockwise until reaching the 3' end. The variant of interest, located at position 21, is indicated by a red mark

positioned on the top of the mutant circular plot. Higher probabilities are represented by darker gray scales. The dot plot on the right of circos shows the differences in base pairing probabilities between the mutated and wild-type RNA  $Pr(bp \text{ in WT}) - Pr(bp \text{ in mut})$ . In this, base pairs weakened by the mutation are shaded in blue, while regions exhibiting increased base pair probabilities in the mutant are highlighted in red. The accessibility profiles of WT and MT RNA sequences, in terms of unpaired probabilities, are depicted on the right. The blue line illustrates the variations in accessibility (WT-mut), where negative values indicate positions more prone to being unpaired in the mutant compared to the wild type (WT).

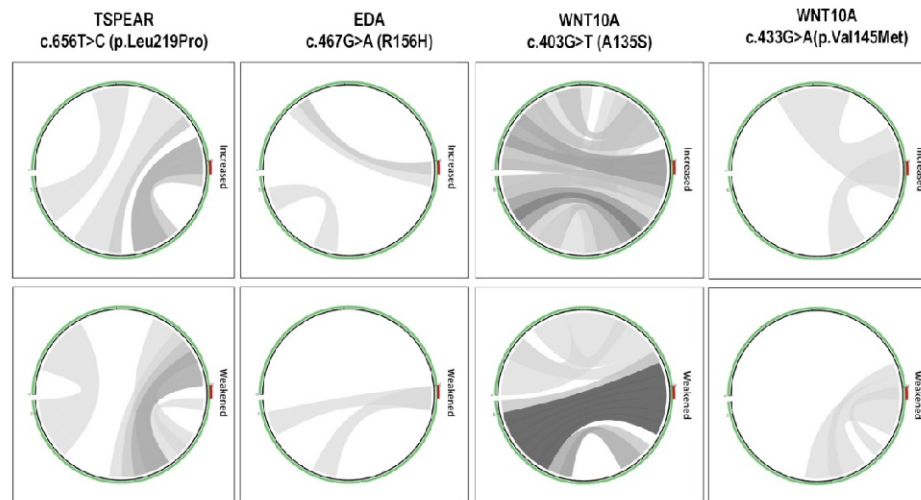


**Figure 7: Comparative Visualization Effects.** The comparative figure aid in the easy identification and comparison of mutation effects. Right and left circus represent the increased base pairs and weakened base pairs probabilities between the nucleotides within the RNA sequence. Darker shades of gray indicate higher absolute changes. The variant position is marked by a red bar in the plot.



**Figure 8: Conservation Analysis of Gene Variants Across WNT10A, PAX9, EDA, and TSPEAR**

The figure illustrates the conservation analysis of gene variants across four key genes: WNT10A, PAX9, EDA, and TSPEAR. The sequence alignment highlights regions of variability and conservation using a color-coded scheme. Highly conserved regions are marked in dark pink, indicating sequence stability and potential functional importance. Less conserved or variable regions are shown in shades of blue and teal, with lighter colors reflecting higher variability. Yellow segments indicate areas with insufficient data for reliable analysis. Red boxes outline specific regions containing variants of interest, emphasizing their positions within the protein sequences. This visual representation helps in understanding the evolutionary conservation of these variants, which is crucial for assessing their potential functional impacts and roles in related biological processes.

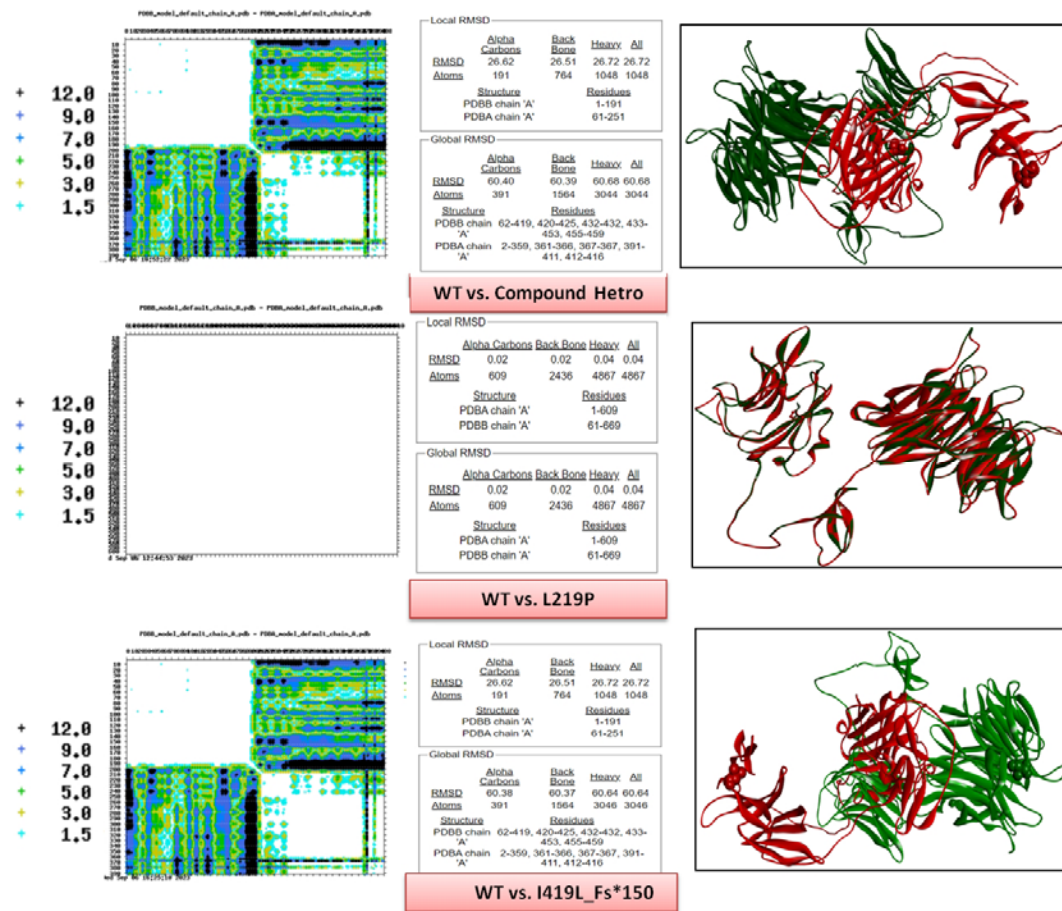


**Figure 9:** Comparative Analysis of TSPEAR Variants Through Matrix Plot and 3D Structural Evaluation. Left Panel: Matrix plot comparing wild-type (WT) and mutant (compound heterozygous and L219P) variants of TSPEAR. Color intensity indicates the extent of structural alterations, with darker shades representing greater structural changes and lighter shades indicating minimal or no changes. Middle Panel: Local and global RMSD (Root Mean Square Deviation) values for the full-length protein, comparing structural deviations across wild-type and mutant variants. Right Panel: 3D structural representations of the TSPEAR variants, with color-coding to denote regions of significant structural differences. Wild-type regions are shown in green, while mutations are highlighted in red. These analyses underscore the impact of mutations on protein stability, flexibility, and interactions, offering insights into the potential functional consequences of these variants.

It is made available under a [CC-BY-NC-ND 4.0 International license](https://creativecommons.org/licenses/by-nc-nd/4.0/).

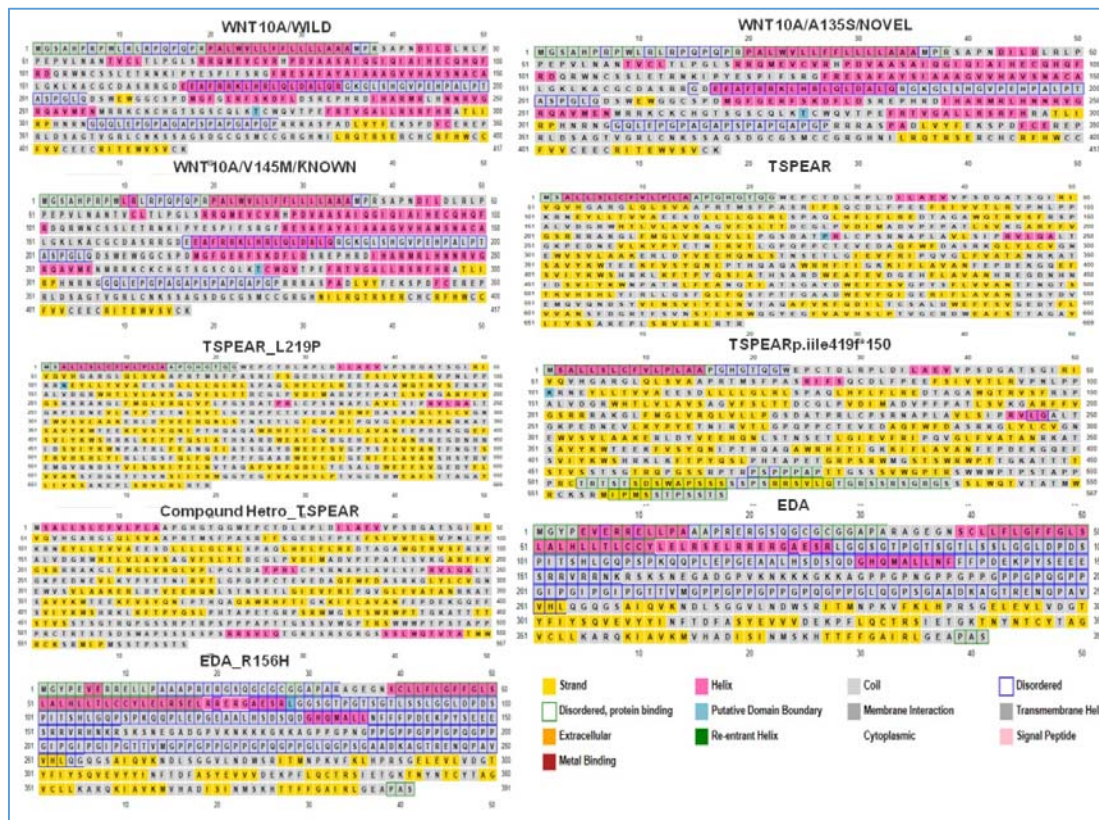


**Figure 10: Secondary Structure Prediction of Variants in WNT10A, TSPEAR, and EDA**

The figure illustrates the secondary structure prediction of protein variants in the WNT10A, TSPEAR, and EDA genes, highlighting alterations caused by specific mutations. **WNT10A Variants:** Comparisons between wild-type (WILD), known variant (p.V145M), and novel variant (p.A135S). Structural elements like helices, strands, and metal-binding regions are shown, with changes indicating potential structural impact of the variants. **TSPEAR Variants:** Displays predicted structures for p.L219P, compound heterozygous mutations, and a frameshift mutation (p.Ile419Lfs\*150). Variants are assessed for alterations in structural domains, including transmembrane helices and signal peptides. **EDA Variants:** Shows secondary structure predictions for the wild-type and p.R156H variant, highlighting potential alterations in metal-binding and extracellular domains. Color coding represents different structural features, such as strands, helices, and metal-binding regions, offering insight into how specific mutations might disrupt or alter protein structure and function.



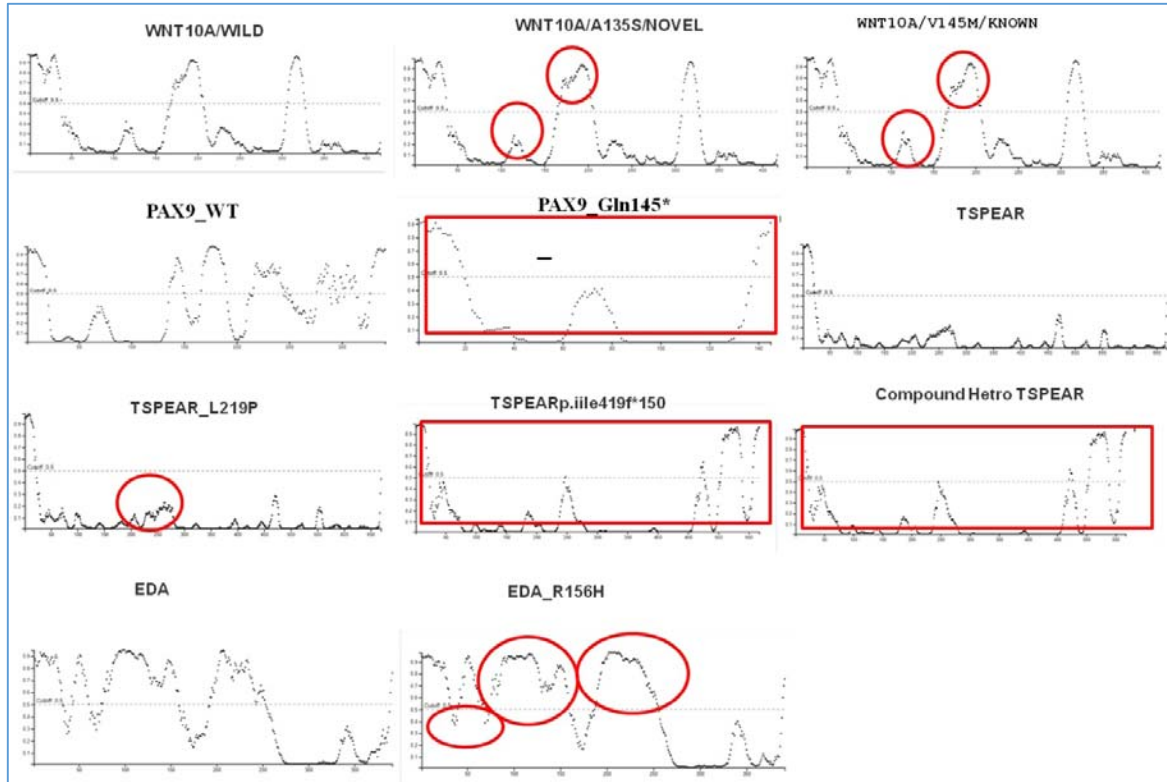


**Figure 11: Protein Disorder Prediction of Variants in WNT10A, TSPEAR, and EDA**

The figure presents the protein disorder prediction analysis for variants in the WNT10A, TSPEAR, and EDA genes, comparing structural changes between wild-type and mutant forms. **WNT10A Variants:** Disorder profiles for the wild-type, known variant (p.V145M), and novel variant (p.A135S) are depicted. Changes in disorder regions may suggest alterations in protein flexibility or functional sites. **TSPEAR Variants:** Disorder analysis includes p.L219P, compound heterozygous mutations, and frameshift mutation (p.Ile419Lfs\*150). Variations in disordered regions highlight the potential impact on protein stability and interaction domains. **EDA Variants:** Displays predicted disorder patterns for wild-type and p.R156H mutant. Differences in disordered segments may affect protein functionality and binding capabilities.

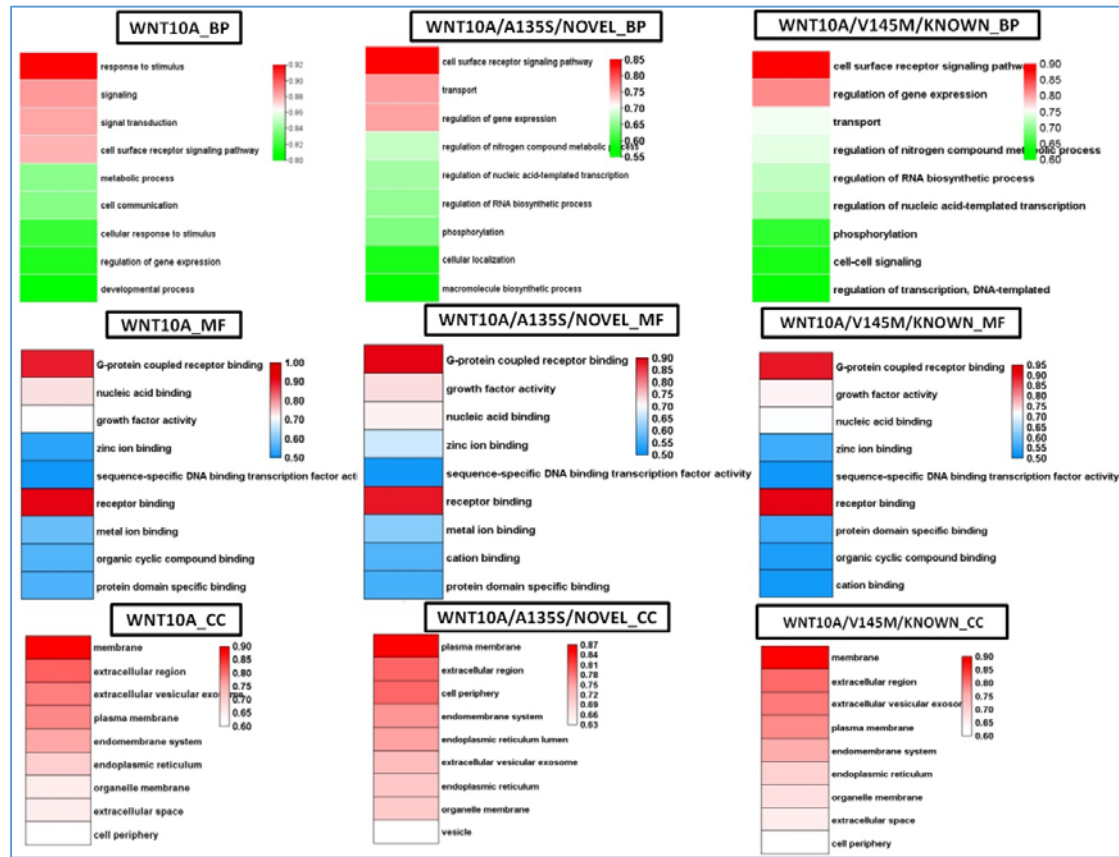


**Figure 12: GO enrichment analysis of WNT10A variants.** The figure displays the GO enrichment results for three biological processes (BP), molecular functions (MF), and cellular components (CC) associated with WNT10A wild-type (WT), A135S, and V145M variants. The heatmap represents the enrichment score (y-axis) for each GO term (x-axis). The color intensity indicates the significance of the enrichment, with red representing higher significance and blue representing lower significance. The results highlight the functional differences among the WNT10A variants, particularly in terms of their involvement in signaling pathways, cell processes, and molecular functions.

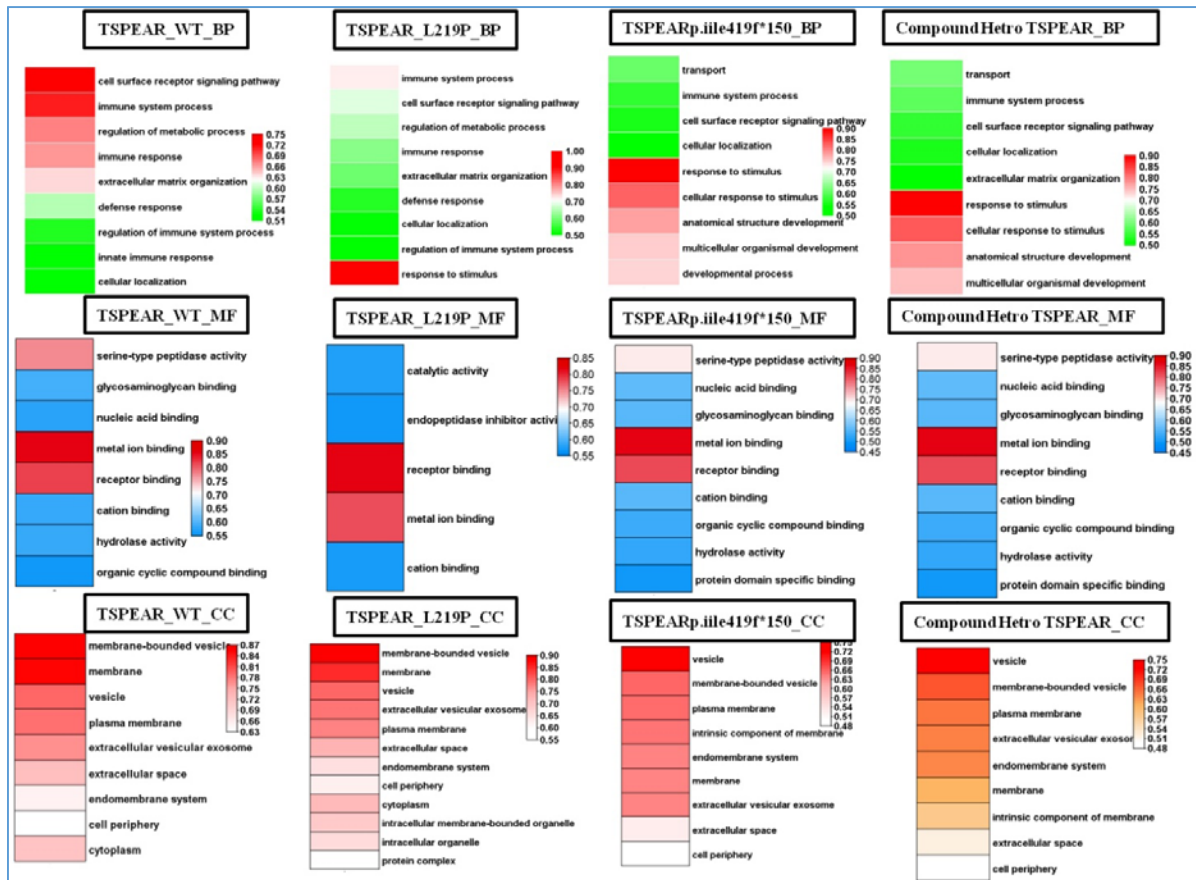


**Figure 13: Gene Ontology (GO) enrichment analysis of TSPEAR variants.** The figure displays the GO enrichment results for three biological processes (BP), molecular functions (MF), and cellular components (CC) associated with TSPEAR wild-type (WT), L219P, I419f\*150 variants, and their compound heterozygous state. The heatmap represents the enrichment score (y-axis) for each GO term (x-axis). The color intensity indicates the significance of the enrichment, with red representing higher significance and blue representing lower significance. The results highlight the functional differences among the TSPEAR variants, particularly in terms of their involvement in immune system processes, cell surface receptor signaling, and extracellular matrix organization.



**Figure 14: GO enrichment analysis of PAX9 variants.** The figure displays the GO enrichment results for three biological processes (BP), molecular functions (MF), and cellular components (CC) associated with PAX9 wild-type (WT) and Gln145\* variant. The heatmap represents the enrichment score (y-axis) for each GO term (x-axis). The color intensity indicates the significance of the enrichment, with red representing higher significance and blue representing lower significance. The results highlight the functional differences between the PAX9 variants, particularly in terms of their involvement in gene expression regulation, transcription, and nuclear processes.



**Figure 15: GO enrichment analysis of EDA variants.** The figure displays the GO enrichment results for three biological processes (BP), molecular functions (MF), and cellular components (CC) associated with EDA wild-type (WT) and R156H variant. The heatmap represents the enrichment score (y-axis) for each GO term (x-axis). The color intensity indicates the significance of the enrichment, with red representing higher significance and blue representing

lower significance. The results highlight the functional differences between the EDA variants, particularly in terms of their involvement in cell signaling, receptor binding, and membrane components.

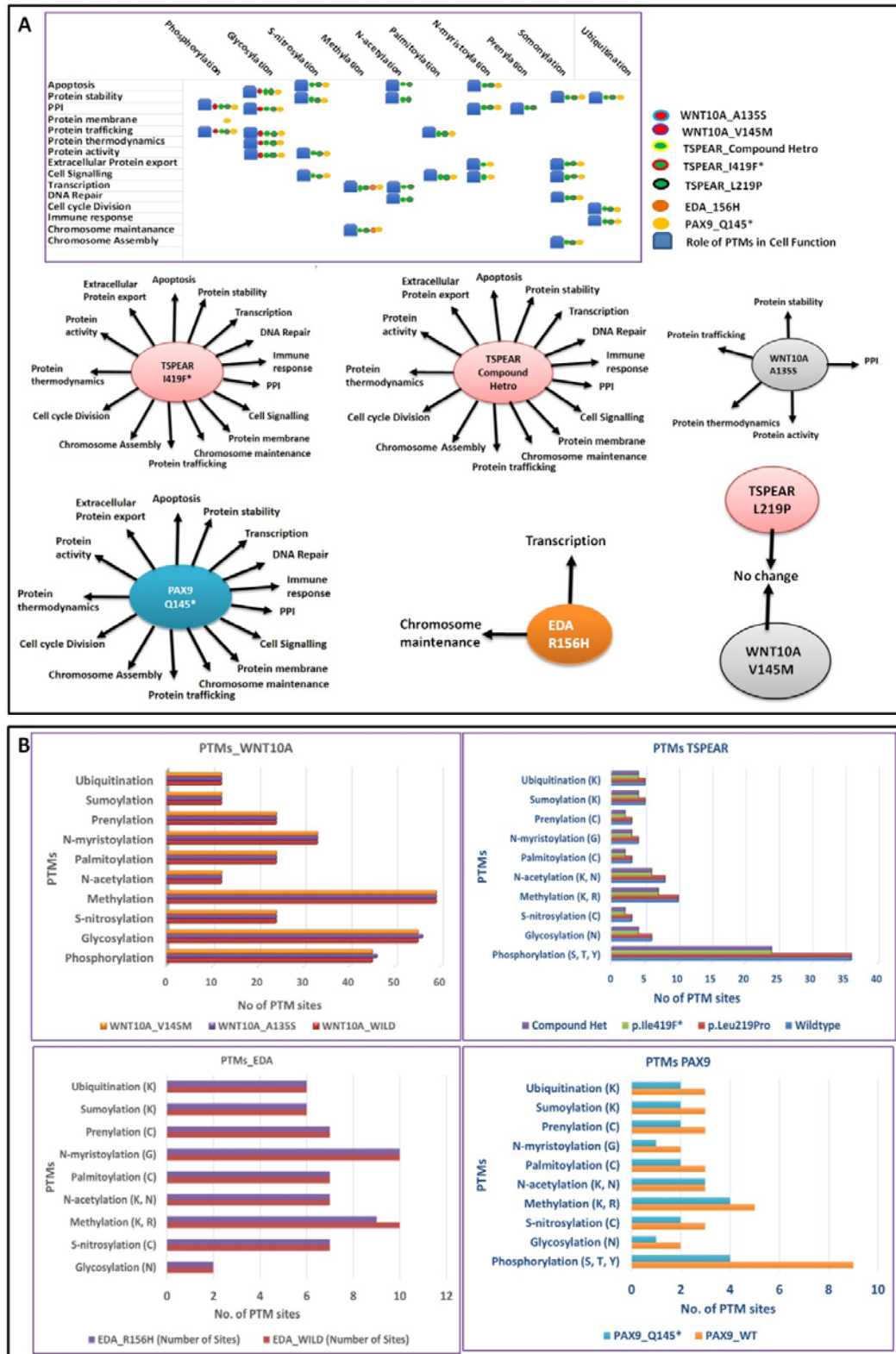


**Figure 16: Post-Translational Modifications (PTMs) Enrichment Analysis of WNT10A, EDA, PAX9, and TSPEAR Variants.** The figure illustrates the enrichment patterns of different PTMs (such as phosphorylation, ubiquitination, acetylation, etc.) associated with the wild-type (WT) and mutant forms of these genes. **(A)** Highlights the changes in PTMs observed in the variants and their potential functional impacts. **(B)** Shows the fluctuations in PTM levels, comparing the wild-type to the mutant variants, emphasizing variations in PTM profiles.



**Figure 17: Subcellular localization analysis of WNT10A, EDA, PAX9, and TSPEAR variants.** The figure depicts the predicted subcellular localization probabilities for each variant across various organelles (a-d) (peroxisome, Golgi apparatus, lysosome/vacuole, endoplasmic reticulum, plastid, mitochondrion, cell membrane, extracellular space, nucleus, and cytoplasm). (e) The PCA plot illustrates the clustering of protein variants based on cellular localization profiles. EDA wild-type and R156H variant cluster closely, indicating minimal changes in localization. PAX9 wild-type and Q145\* variant show slight shifts, suggesting potential alterations. WNT10A wild-type and p.V145M variant cluster together, reflecting little change. TSPEAR variants, including the compound heterozygous and L219P, display distinct positions, indicating significant differences in cellular localization. Overall, most variants show similar localization patterns to wild-type, except for notable shifts in TSPEAR variants, which may affect functionality.

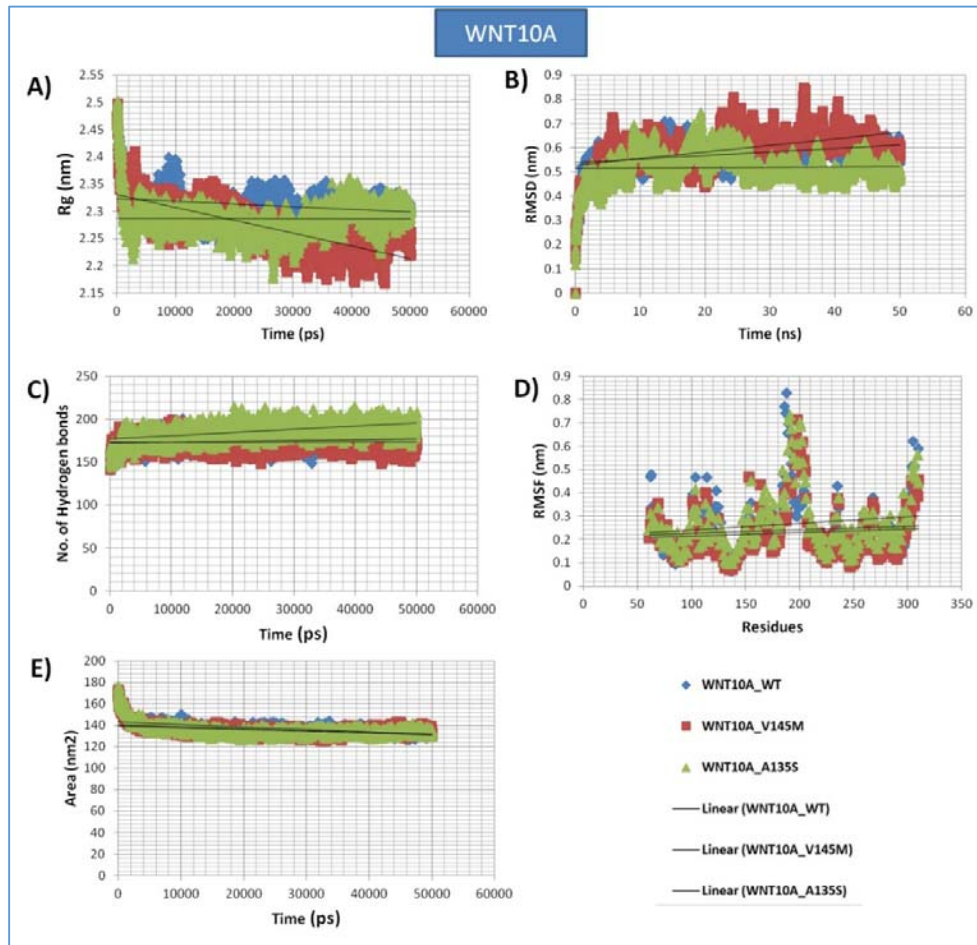


**Figure 18: Molecular dynamics simulation analysis of WNT10A variants.** The figure depicts the time evolution of various structural and dynamic properties for wild-type (WT) and mutant WNT10A proteins (V145M and A135S). **A:** Radius of gyration (Rg) over time. The graph shows the Rg values over time for WNT10A wild-type (WT), V145M, and A135S variants. The Rg values indicate the compactness of the protein structure, where consistent lower values suggest a more compact structure. WT (blue) shows relatively stable compactness, while variants exhibit fluctuations, with V145M (red) being less stable than A135S (green). **B:** Root-mean-square deviation (RMSD) over time. This panel illustrates the RMSD of the protein backbone over time, reflecting structural stability. WT (blue) maintains lower RMSD, indicating higher stability, whereas V145M (red) shows increased deviation, suggesting structural alterations and reduced stability. A135S (green) remains moderately stable. **C:** Number of hydrogen bonds over time. The number of hydrogen bonds over time is shown for each variant. WT (blue) maintains a higher number of hydrogen bonds, suggesting more stable intramolecular interactions. The variants V145M (red) and A135S (green) show variations, with V145M forming fewer hydrogen bonds, potentially leading to decreased structural stability. **D:** Root-mean-square fluctuation (RMSF) per residue. RMSF values across residues reveal regions of



high flexibility and fluctuation. WT (blue) shows lower fluctuations overall, indicating stable regions, while variants, especially V145M (red), show increased fluctuation at certain residues, pointing to local instability. **E**: SAS over time. The SAS values are plotted over time, where lower values indicate reduced exposure to the solvent. WT (blue) shows consistent lower SAS, suggesting a stable and compact structure. V145M (red) has a higher SAS, reflecting more exposure, while A135S (green) shows intermediate values.

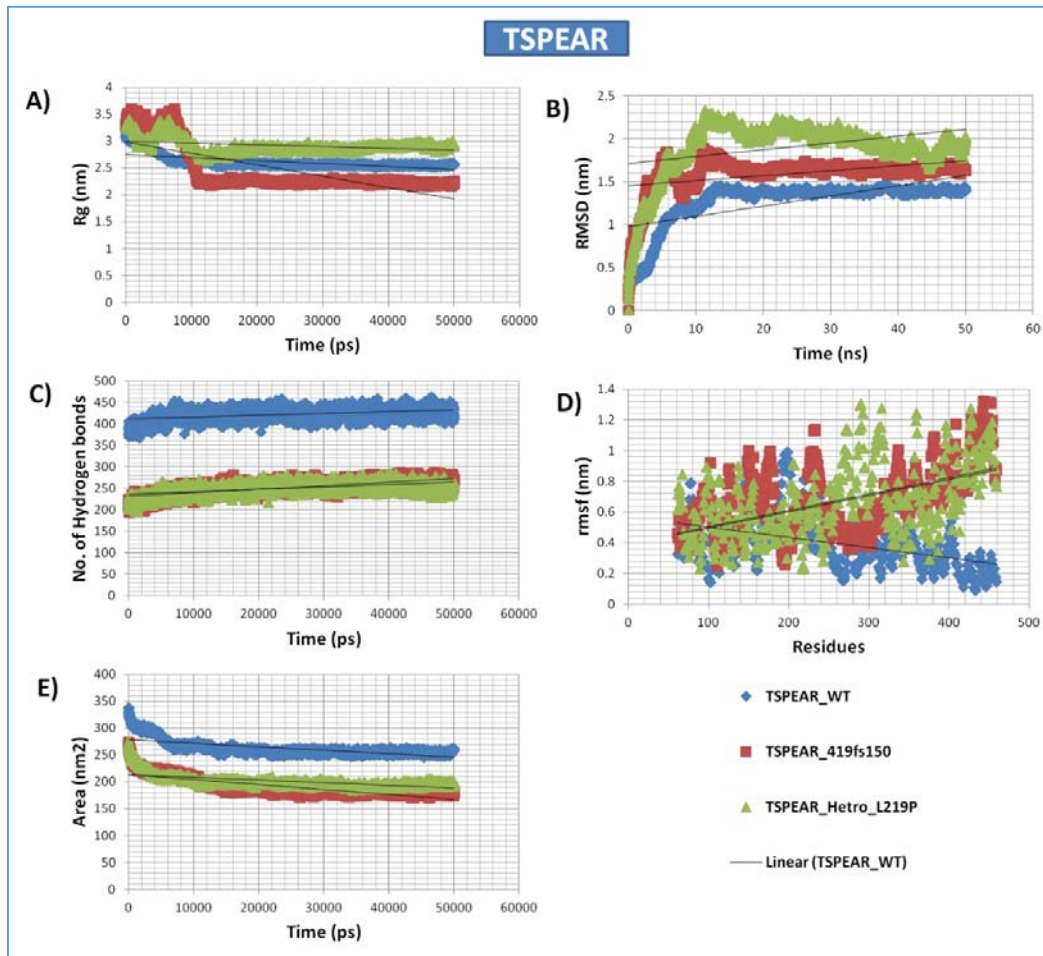


**Figure 19: Molecular dynamics simulation analysis of TSPEAR variants.** The figure depicts the time evolution of various structural and dynamic properties for wild-type (WT), 419fs150, and L219P variants of TSPEAR. **(A) Radius of Gyration (Rg):** This graph represents the Rg values for TSPEAR wild-type (WT), 419fs150, and Hetro\_L219P variants over time, indicating the compactness of each protein structure. The WT (blue) shows a stable Rg, reflecting a consistent compact structure. The 419fs150 variant (red) displays slight fluctuations, while Hetro\_L219P (green) shows more variability, suggesting a less compact and potentially more flexible structure. **(B) Root Mean Square Deviation (RMSD):** RMSD plots reveal structural stability across time. The WT (blue) maintains lower RMSD, indicating a stable structure throughout the simulation. The 419fs150 variant (red) shows moderate deviations, while Hetro\_L219P (green) has higher RMSD values, suggesting increased structural instability and flexibility. **(C) Number of Hydrogen Bonds:** The panel shows the number of hydrogen bonds formed over time. The WT (blue) maintains a higher and consistent number of hydrogen bonds,

suggesting strong intramolecular interactions. The 419fs150 variant (red) shows a similar pattern but with slight reductions, while Hetro\_L219P (green) displays fewer hydrogen bonds, indicating weaker structural cohesion. **(D) Root Mean Square Fluctuation (RMSF):** RMSF values are displayed for each residue, revealing regions of high flexibility and fluctuation. WT (blue) exhibits lower overall fluctuations, showing stable regions throughout the protein. The 419fs150 variant (red) shows moderate fluctuations, and Hetro\_L219P (green) has the highest fluctuations, indicating regions of instability that may impact function. **(E) SAS:** The SAS plot demonstrates the degree of exposure of the protein to the solvent. WT (blue) maintains a relatively lower SAS, reflecting a compact structure. The 419fs150 variant (red) shows slightly higher SAS, and Hetro\_L219P (green) exhibits the highest exposure, suggesting more open and less stable structural conformations.

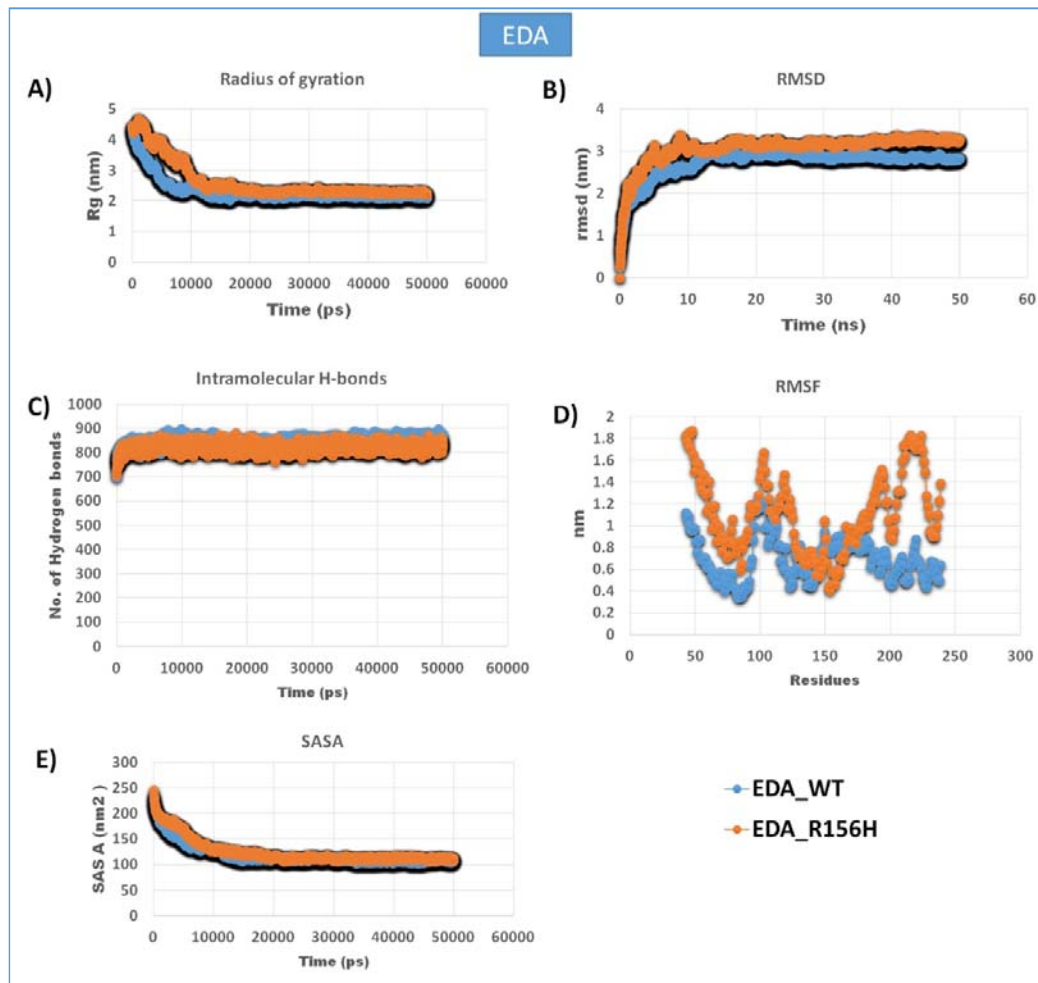


**Figure 20: Molecular dynamics simulation analysis of EDA variants.** The figure depicts the time evolution of various structural and dynamic properties for wild-type (WT) and R156H variants of EDA. **A:** Radius of gyration (Rg) over time. **B:** Root-mean-square deviation (RMSD) over time. **C:** Number of hydrogen bonds over time. **D:** Root-mean-square fluctuation (RMSF) per residue. **E:** SASA over time. The different line colors represent the different EDA variants, allowing for comparison of their structural and dynamic behavior. The results highlight potential differences in protein stability, flexibility, and interactions due to the R156H mutation.

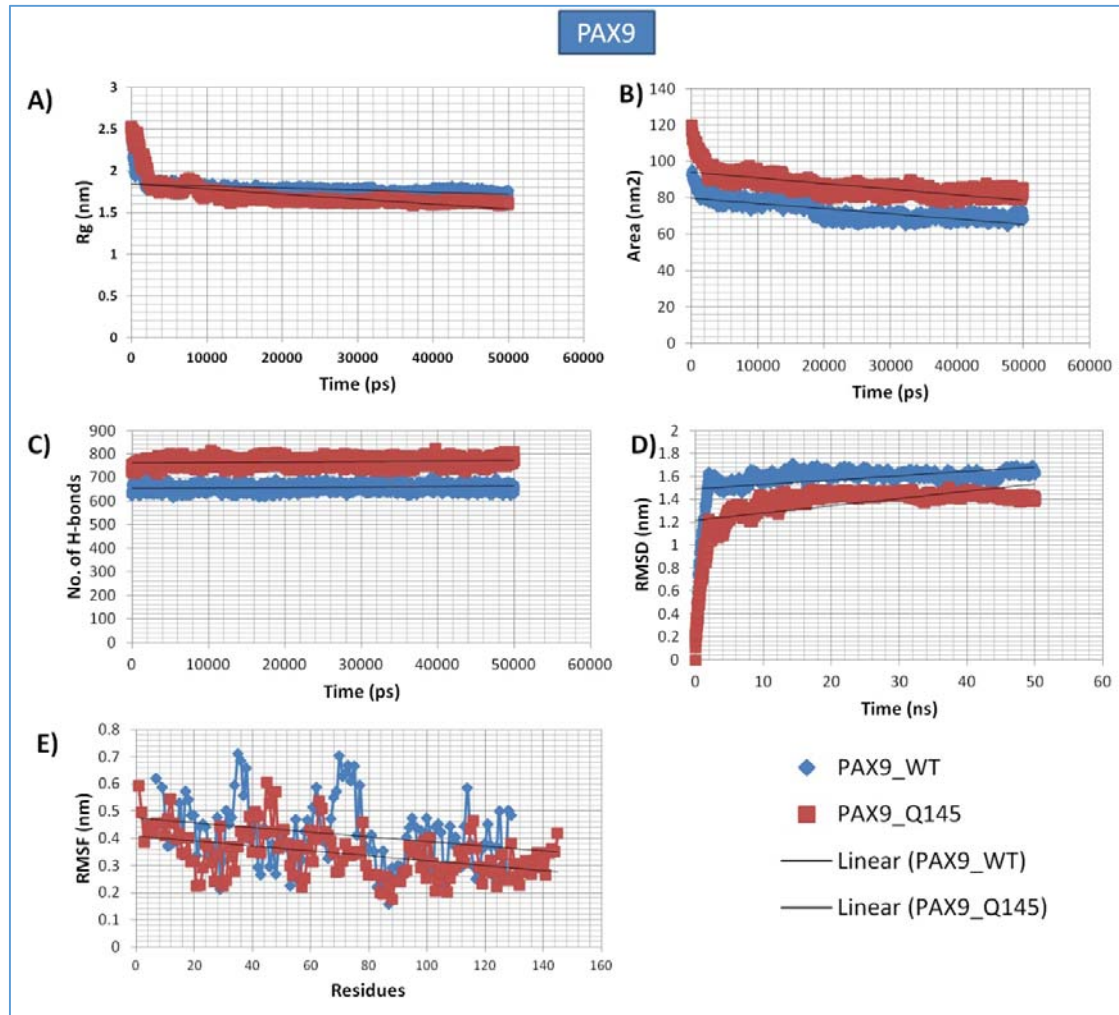


**Figure 21: Molecular dynamics simulation analysis of PAX9 variants.** The figure depicts the time evolution of various structural and dynamic properties for wild-type (WT) and Q145\* variants of PAX9. **A:** Radius of gyration (Rg) over time. **B:** SAS analysis over time. **C:** Number of hydrogen bonds over time. **D:** Root-mean-square deviation (RMSD) over time. **E:** Root-mean-square fluctuation (RMSF) per residue. The different line colors represent the different PAX9 variants, allowing for comparison of their structural and dynamic behavior. The results highlight potential differences in protein stability, flexibility, and interactions due to the Q145\* mutation.

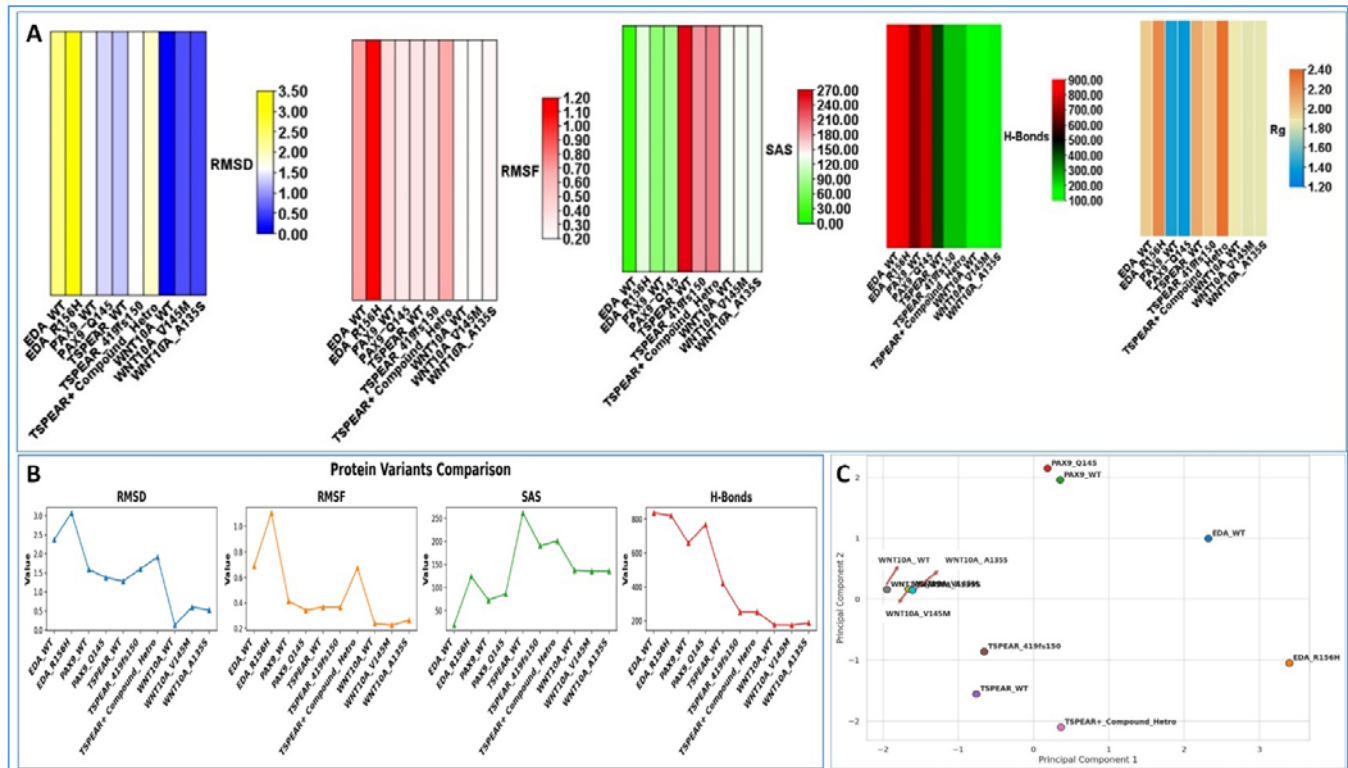


**Figure 22: Comparative analysis of protein dynamics and stability for WNT10A, EDA, PAX9, and TSPEAR variants.** A. The figure displays the results of molecular dynamics simulations, including: **RMSD**: indicating the overall structural stability of the protein. **RMSF**: revealing the flexibility of different regions within the protein. **SAS**, reflecting the protein's exposure to solvent. **Rg** measuring the protein's compactness. **Hydrogen bonds**: The number of hydrogen bonds formed within the protein. The color gradients in each plot represent the different variants, allowing for a visual comparison of their dynamic properties. The results highlight potential differences in protein stability, flexibility, and interactions due to the mutations. B. Matplot for simulated variants. C. Principal Component Analysis (PCA) of Variants and Wild-Type Proteins. The scatter plot shows the PCA results for wild-type (WT) and variant forms of PAX9, WNT10A, TSPEAR, and EDA proteins. Each point represents a different protein or variant, positioned based on their principal component 1 (PC1) and principal component 2 (PC2) scores, indicating the degree of structural variation. Wild-type proteins are labeled with "WT," while variants are denoted by specific mutations (e.g., PAX9\_Q145, EDA\_R156H). The plot highlights clustering of WT and mutant proteins, illustrating how structural differences influence their positions in the principal component space, reflecting variations in protein stability, conformation, and functionality. Matplotlib, providing a clear representation of the dynamic properties of the simulated variants.